

BULLETIN N° 241
ACADÉMIE EUROPÉENNE
INTERDISCIPLINAIRE
DES SCIENCES
INTERDISCIPLINARY EUROPEAN ACADEMY OF SCIENCES



Lundi 6 janvier 2020 à 17h
à l'Institut Curie, Amphi BURG salle annexe 2
12, rue Lhomond 75005 PARIS

Conférence:

"Comment les microbes structurent notre monde"

par Marc André SELOSSE

Professeur au Muséum national d'Histoire naturelle

Professeur invité aux universités de Gdansk (Pologne) et Kunming (Chine)

Responsable de l'Équipe Interactions et Évolution Végétale et Fongique

Institut de Systématique, Évolution, Biodiversité

UMR 7205 MNHN-CNRS-SU-EPHE-UA45

Notre Prochaine séance aura lieu le lundi 3 février 2020 à 17h

à l'Institut Curie, Amphi BURG salle annexe 2

12, rue Lhomond 75005 PARIS

Elle aura pour thème

Conférence:

" Des circuits électriques quantiques "

par Daniel ESTÈVE

Directeur de Recherche au CEA

Membre de l'Académie des Sciences

Quantronique, Service de Physique de l'Etat Condensé, CEA-Saclay

Académie Européenne Interdisciplinaire des Sciences

Siège Social : 5 rue Descartes 75005 Paris

Nouveau Site Web : <http://www.science-inter.com>

ACADÉMIE EUROPÉENNE INTERDISCIPLINAIRE DES SCIENCES INTERDISCIPLINARY EUROPEAN ACADEMY OF SCIENCES

PRÉSIDENT : Pr Victor MASTRANGELO
VICE PRÉSIDENT : Pr Jean-Pierre FRANÇOISE
VICE PRÉSIDENT BELGIQUE(Liège):
 Pr Jean SCHMETS
VICE PRÉSIDENT ITALIE(Rome):
 Pr Ernesto DI MAURO
VICE PRÉSIDENT Grèce (Athènes)
 Anastassios METAXAS

SECRÉTAIRE GÉNÉRALE : Irène HERPE-LITWIN
TRÉSORIÈRE GÉNÉRALE: Édith PERRIER

MEMBRES CONSULTATIFS DU CA :
 Gilbert BELAUBRE
 François BÉGON
 Bruno BLONDEL
 Michel GONDRAN

PRÉSIDENT FONDATEUR : Dr. Lucien LÉVY (†)
PRÉSIDENT D'HONNEUR : Gilbert BELAUBRE

CONSEILLERS SCIENTIFIQUES :
SCIENCES DE LA MATIÈRE : Pr. Gilles COHEN-TANNOUJJI
SCIENCES DE LA VIE ET BIOTECHNIQUES : Pr Ernesto DI MAURO

CONSEILLERS SPÉCIAUX:
ÉDITION: Pr Robert FRANCK
RELATIONS EUROPÉENNES :Pr Jean SCHMETS
RELATIONS avec AX: Gilbert BELAUBRE
RELATIONS VILLE DE PARIS et IDF:
 Michel GONDRAN et Claude MAURY
MOYENS MULTIMÉDIA et UNIVERSITÉS: Pr Alain CORDIER
RECRUTEMENTS: Pr. Sylvie DERENNE
SYNTHÈSES SCIENTIFIQUES: Jean-Pierre TREUIL
MECENAT: Pr Jean Félix DURASTANTI
**GRANDS ORGANISMES DE RECHERCHE NATIONAUX ET
 INTERNATIONAUX**: Pr Michel SPIRO
THÈMES ET PROGRAMMES DE COLLOQUES: Pr Jean SCHMETS

SECTION DE NANCY :
PRESIDENT : Pr Pierre NABET

janvier 2020

N°241

TABLE DES MATIERES
 p. 03 Séance du 6 janvier 2020 :
 p. 06 Documents

Prochaine séance : lundi 3 février 2020

Conférence:
"Des Circuits électriques Quantiques"
 par **Daniel ESTÈVE**
Directeur de Recherche au CEA
 Membre de l'Académie des Sciences
 Quantronique, Service de Physique de l'Etat Condensé, CEA-Saclay

ACADEMIE EUROPEENNE INTERDISCIPLINAIRE DES SCIENCES

Fondation de la Maison des Sciences de l'Homme, Paris.

Séance du Lundi 6 janvier/Institut Curie 17h

La séance est ouverte à 17h sous la Présidence de Victor MASTRANGELO et en la présence de nos Collègues Gilbert BELAUBRE(?), Jean BERBINAU, Eric CHENIN, Françoise DUTHEIL, Claude ELBAZ, Irène HERPE-LITWIN, Claude MAURY, Marie-Françoise PASSINI, Jacques PRINTZ, Jean SCHMETS, Jean-Pierre TREUIL.

Etait également présent notre collègue, membre correspondant Benoît PRIEUR.

Etaient excusés : François BEGON, Jean-Pierre BESSIS, Bruno BLONDEL, Jean-Louis BOBIN, Michel CABANAC, Alain CARDON, Juan-Carlos CHACHQUES, Gilles COHEN-TANNOUDJI, Alain CORDIER, Daniel COURGEAU, Sylvie DERENNE, Ernesto DI MAURO, Jean-Félix DURASTANTI, Vincent FLEURY, Robert FRANCK, Jean -Pierre FRANCOISE, Michel GONDRAN, Dominique LAMBERT, Pierre MARCHAIS, Anastassios METAXAS, Jacques NIO, Pierre PESQUIES, Edith PERRIER, Denise PUMAIN, René PUMAIN, Michel SPIRO, Alain STAHL

I. Conférence du Pr Marc André SELOSSE

A. Présentation du conférencier

Marc-André SELOSSE est professeur du Muséum national d'Histoire naturelle et professeur invité aux universités de Gdansk (Pologne) et Kunming (Chine). Ses recherches portent sur l'écologie et l'évolution des associations à bénéfices mutuels (symbioses). Mycologue et botaniste, il travaille en particulier sur les symbioses mycorhiziennes qui unissent des champignons du sol aux racines des plantes. Il s'intéresse à la diversité spécifique et génétique des champignons impliqués, et à l'évolution de ces symbioses (notamment chez les orchidées). Il enseigne dans diverses formations universitaires et à l'Ecole Normale Supérieure et contribue à diverses formations des enseignants. Vice-président de la Société Botanique de France et membre correspondant de l'Académie d'Agriculture, il est éditeur de quatre revues scientifiques internationales (*Symbiosis*, *The New Phytologist*, *Ecology Letters* et *Botany Letters*). Il a publié près d'une centaine d'articles de recherche et autant d'articles de vulgarisation, tous librement téléchargeables en ligne sur son site institutionnel (<http://isyeb.mnhn.fr/fr/annuaire/marc-andre-selosse-404>). Il a publié chez Actes Sud un ouvrage sur la place des microbes dans le monde qui nous entoure, « *Jamais seul : ces microbes qui construisent les plantes, les animaux et les civilisations* » (2017), et un autre sur les tannins qui accompagnent nos vies, « *Les goûts et les couleurs du monde. Une histoire naturelle des tannins, de l'écologie à la santé* » (2019).

B. Conférence

Résumé de la conférence:

Comment les microbes structurent notre monde

Pr Marc André SELOSSE

Une double révolution a émergé en biologie en ce début de XXIème siècle : les microbes sont partout, et ils tissent, au-delà des maladies ou de la décomposition, des relations vitales, à bénéfices mutuels, avec les plus gros organismes.

Les plantes ne peuvent pas vivre sans microbes, bactéries ou champignons : elles en contiennent jusque dans leurs cellules ! Les animaux, à commencer par nous-mêmes, ne seraient pas ce qu'ils sont sans les microbes qui les colonisent : intestin, mais aussi peau et tous nos cavités sont défendues par des microbes... qui influent jusque sur le comportement (et vous en découvrirez de belles sur la nature microbienne de... l'allaitement !).

Même notre évolution culturelle s'est appuyée sur des microbes, par exemple dans l'émergence de l'alimentation moderne (laitages, plantes domestiquées, etc.). Aujourd'hui, comprendre cette présence dégage des leviers pour la santé, la production alimentaire et une gestion de notre environnement respectueuse de l'avenir. Négliger le rôle des microbes peut, au rebours, entraîner des problèmes comme l'essor des allergies, de l'obésité, ou encore de tragiques erreurs d'ingénierie environnementale.

Plantes, animaux et écosystèmes ne sont « jamais seuls », venez découvrir comment les microbes bâtissent le monde qui nous entoure !

Un compte-rendu rédigé par un membre de l'AEIS sera prochainement disponible sur le site de l'AEIS <http://www.science-inter.com>.

REMERCIEMENTS

Nous tenons à remercier vivement M. Jean-Louis DUPLOYE et M. Yann TRAN de l'Institut Curie pour la qualité de leur accueil.

Annances

1. Notre collègue André FRATINI annonce la sortie en kiosque du N°22 du Mag culturel **Rebelle(s)** dans lequel se trouve son article :

Le complexe de Dédale : <https://rebelles-lemag.com/2020/01/13/rebelles-mag-n22-controle-social-flics-et-robots-a-la-decheterie/>

2. Notre collègue d'Athènes Anastassios Ioannis METAXAS nous communique le calendrier des Rencontres Interdisciplinaires Franco-Helleniques, société savante associée à l'AEIS , dont le siège est situé 154 rue Asklipiou 114 71 ATHÈNES :

“KTIRIO KOSTIS PALAMAS”

CALENDRIER DES SEANCES

2019-2020

Chaque séance débutera à 19h00 précises

(1)

Mercredi 11 décembre 2019, Cécile INGLESSIS MARGELLOS

Croisements : La traduction en tant qu'interdisciplinarité, l'interdisciplinarité en tant que traduction.

(2)

Jeudi 23 janvier 2020, Dimitris APOSTOLOPOULOS

Demandes interdisciplinaires dans l'histoire postbyzantine.

(3)

Mercredi 26 février 2020, Panayiotis TOURNIKIOTIS

Pour une Architecture Interdisciplinaire.

(4)

Mercredi 18 mars 2020, Pavlos SOURLAS

Philosophie et Biologie. Réflexions sur une rencontre attendue.(5)

Jeudi 30 avril 2020, Denis ZACHAROPOULOS

La grandeur inconnue des modalités et de la raison d'être des oeuvres. Appel à l'interdisciplinarité.

(6)

Mercredi 6 mai 2020, Andreas CAPETANIOS

Les topos de l'archéologie. De la coexistence des méthodologies à l'interdisciplinarité.

(7)

Mercredi 27 mai 2020, Dionissios KOKKINOS

La médecine comme art.

(8)

Mercredi 24 juin 2020, Vana XENOU

Sur la déconstruction des mécanismes de représentation.

Actions et relations vécues interférant entre la théorie et la créativité

Documents

Pour préparer la conférence de Daniel ESTÈVE :

p.07 : le résumé en français de sa présentation

p.08 : Un article intitulé " Antibunched Photons Emitted by a dc-Biased Josephson Junction",
Rolland, C. et al., paru dans PHYSICAL REVIEW LETTERS 122, 186804, 2019;

p.36: Un article intitulé : Inductive-detection electron-spin resonance spectroscopy with 65 spins/root
Hz sensitivity, Probst, S. et al., APPLIED PHYSICS LETTERS 111, 202604, 2017;

Circuits électriques via la mécanique quantique

Daniel Estève,

Directeur de recherche CEA

Membre de l'Académie des Sciences

Quantronique, Service de Physique de l'État Condensé, CEA-Saclay

Tout système physique étant capable en théorie d'atteindre le régime quantique, la recherche des propriétés quantiques des systèmes non-microscopiques s'est considérablement développée pour les variables mécaniques ou les nano-objets et pour les variables électriques des circuits supraconducteurs non dissipatifs.

La découverte au milieu des années 90 selon laquelle la mécanique quantique fournit des moyens de réalisation de tâches de calcul dépassant celles des ordinateurs classiques a provoqué une recherche intense dans le domaine des unités de base, notamment les circuits de bits quantiques nécessaires à la réalisation d'un ordinateur quantique. Je décrirai les bits quantiques les plus avancés et les processeurs quantiques élémentaires réalisés avec. J'expliquerai le problème de flexibilité (scalabilité) pour réaliser un ordinateur quantique intéressant et les solutions envisageables. J'introduirai une route hybride basée sur les spins microscopiques couplés aux circuits électriques quantiques qui sont développés actuellement dans notre équipe.

See discussions, stats, and author profiles for this publication at: <https://www.researchgate.net/publication/328303575>

Antibunched Photons Emitted by a dc-Biased Josephson Junction

Preprint in Physical Review Letters · October 2018

DOI: 10.1103/PhysRevLett.122.186804

CITATIONS

5

READS

136

13 authors, including:



Chloé Rolland

Atomic Energy and Alternative Energies Commission

11 PUBLICATIONS 62 CITATIONS

SEE PROFILE



Marc Peter Westig

Grünecker Patent- und Rechtsanwälte PartG mbB

31 PUBLICATIONS 96 CITATIONS

SEE PROFILE



Björn Kubala

Ulm University

38 PUBLICATIONS 918 CITATIONS

SEE PROFILE



Carles Altimiras

Atomic Energy and Alternative Energies Commission

23 PUBLICATIONS 693 CITATIONS

SEE PROFILE

Some of the authors of this publication are also working on these related projects:



Control of single electrons [View project](#)



spin control [View project](#)

Antibunched photons emitted by a dc-biased Josephson junction

C. Rolland^{1,*}, A. Peugeot^{1,*}, S. Dambach², M. Westig¹, B. Kubala², Y. Mukharsky¹, C. Altimiras¹, H. le Sueur¹, P. Joyez¹, D. Vion¹, P. Roche¹, D. Esteve¹, J. Ankerhold^{2,†} and F. Portier^{1,‡}

¹ SPEC (UMR 3680 CEA-CNRS), CEA Paris-Saclay, 91191 Gif-sur-Yvette, France and

² Institute for Complex Quantum Systems and IQST, University of Ulm, 89069 Ulm, Germany

(Dated: October 16, 2018)

We show experimentally that a dc biased Josephson junction in series with a high-enough impedance microwave resonator emits antibunched photons. Our resonator is made of a simple micro-fabricated spiral coil that resonates at 4.4 GHz and reaches a 1.97 k Ω characteristic impedance. The second order correlation function of the power leaking out of the resonator drops down to 0.3 at zero delay, which demonstrates the antibunching of the photons emitted by the circuit at a rate of 6 $\times 10^7$ photons per second. Results are found in quantitative agreement with our theoretical predictions. This simple scheme could offer an efficient and bright single-photon source in the microwave domain.

PACS numbers: 74.50+r, 73.23Hk, 85.25Cp

Single photon sources constitute a fundamental resource for many quantum information technologies, notably secure quantum state transfer using flying photons. In the microwave domain, although photon propagation is more prone to losses and thermal photons present except at extremely low temperature, applications can nevertheless be considered [1]. Single microwave photons were first demonstrated in [2] using the standard design of single-photon emitters: an anharmonic atom-like quantum system excited from its ground state relaxes by emitting a single photon on a well-defined transition before it can be excited again. The first and second order correlation functions of such a source [3] demonstrate a rather low photon flux limited by the excitation cycle duration, but an excellent antibunching of the emitted photons. In this work, we follow a different approach, where the tunnelling of discrete charge carriers through a quantum coherent conductor creates photons in its embedding circuit. The resulting quantum electrodynamics of this type of circuits [4–10] has been shown to provide e.g. masers [11–14], simple sources of non-classical radiation [15–17], or near quantum-limited amplifiers [18]. When the quantum conductor is a Josephson junction, dc biased at voltage V in series with a linear microwave resonator, exactly one photon is created in the resonator each time a Cooper pair tunnels through the junction, provided that the Josephson frequency $2eV/h$ matches the resonator's frequency [19]. We demonstrate here that in the strong coupling regime between the junction and the resonator, the presence of a single photon in the resonator inhibits the further tunneling of Cooper pairs, leading to the antibunching of the photons leaking out of the resonator [20, 21]. Complete antibunching is expected when the characteristic impedance of the resonator reaches $Z_c = 2R_Q/\pi$, with $R_Q = h/(2e)^2 \simeq 6.45$ k Ω the superconducting resistance quantum. This regime, for which the analogue of the fine structure constant of the problem is of order 1, has

recently attracted attention [22, 23], as it allows the investigation of many-body physics with photons [24, 25] or ultra-strong coupling physics [26], offering new strategies for the generation of non classical radiation [27].

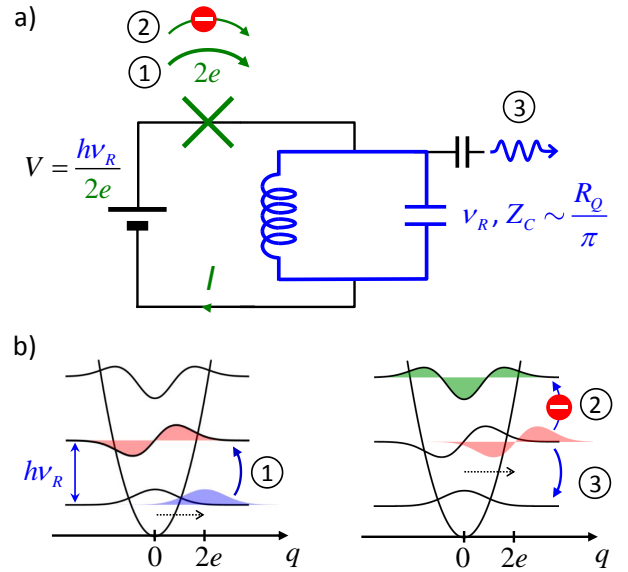


FIG. 1: Principle of the experiment: (a) A Josephson junction in series with a resonator of frequency ν_R and characteristic impedance Z_c of the order of the quantum of resistance is voltage biased so that each Cooper pair that tunnels produces a photon in the resonator (1). (b) Photon creation and relaxation events sketched on the resonator energy diagram. According to DCB theory, a tunneling Cooper pair shifts the charge on the resonator capacitance by $2e$, and the tunneling rate $\Gamma_{n \rightarrow n+1}$ starting with the resonator in Fock state $|n\rangle$ is proportional to the overlap between the wavefunction $\Psi_n(q)$ shifted by $2e$ and $\Psi_{n+1}(q)$. This overlap depends itself on r via the curvature of the electrostatic energy. At a critical Z_c , $\Gamma_{1 \rightarrow 2} = 0$ and no additional photons can be created (2) until the photon already present has leaked out (3). The photons produced are thus antibunched, which is revealed by measuring the $g^{(2)}$ function of the continuous microwave leak.

The simple circuit used in this work is represented in the upper part of Fig. 1: a Josephson junction is coupled to a microwave resonator of frequency ν_R and characteristic impedance Z_c , and biased at a voltage V smaller than the gap voltage $V_{\text{gap}} = 2\Delta/e$, where $-e$ is the electron charge and Δ the superconducting gap, so that single electron tunneling is impossible. The time-dependent Hamiltonian

$$H = (a^\dagger a + 1/2)h\nu_R - E_J \cos[\phi(t)] \quad (1)$$

of the circuit is the sum of the resonator and Josephson Hamiltonians. Here a is the photon annihilation operator in the resonator, E_J is the Josephson energy of the junction, $\phi(t) = 2eVt/\hbar - \sqrt{r}(a + a^\dagger)$ is the phase difference across the junction (conjugate to the number of Cooper pairs transferred across the junction), and $r = \pi Z_c/R_Q$ is the charge-radiation coupling in this one-mode circuit [28]. The nonlinear Josephson Hamiltonian thus couples Cooper pair transfer to photon creation in the resonator. According to the theory of dynamical Coulomb blockade (DCB) [28–30], a dc current can flow in this circuit only when the electrostatic energy provided by the voltage source upon the transfer of a Cooper pair corresponds to the energy of an integer number k of photons created in the resonator: $2eV = kh\nu_R$. Then the steady state occupation number \bar{n} in the resonator results from the balance between the Cooper pair tunneling rate and the leakage rate to the measurement line. For $k = 1$ – the resonance condition of the AC Josephson effect – each Cooper pair transfer creates a single photon. The power

$$\mathcal{P} = \frac{2e^2 E_J^{*2}}{\hbar^2} \text{Re}Z(\nu = 2eV/h) \quad (2)$$

emitted in an empty resonator also coincides with the AC Josephson expression, albeit with a reduced effective Josephson energy $E_J^* = E_J e^{-r/2}$ renormalized by the zero-point phase fluctuations of the resonator [20, 21, 31, 31–34]. In the strong-coupling regime ($r \simeq 1$), however, the single rate description above breaks down as a single photon in the resonator already influences further emission processes, as explained in Fig. 1.

A more sophisticated theory [20, 21] addressing this regime considers the Hamiltonian (1) in the rotating-wave approximation at the resonance condition $2eV = h\nu_R$ for single photon creation. Expressed in the resonator Fock state basis $\{|n\rangle\}$, H reduces to $H^{\text{RWA}} = -(E_J/2) \sum_n (h_{n,n+1}^{\text{RWA}} |n\rangle\langle n+1| + \text{h.c.})$, with the transition matrix elements

$$h_{n,n+1}^{\text{RWA}} = \langle n | \exp[i\sqrt{r}(a^\dagger + a)] | n+1 \rangle. \quad (3)$$

Describing radiative losses via a Lindblad super-operator, one gets the second order coherence function for vanishing occupation number $\bar{n} \ll 1$ [20, 21]:

$$g^{(2)}(\tau) = \frac{\langle a^\dagger(0)a^\dagger(\tau)a(\tau)a(0) \rangle}{\langle a^\dagger a \rangle^2} = \left[1 - \frac{r}{2} \exp(-\kappa\tau/2) \right]^2 \quad (4)$$

with κ the photon leakage rate of the resonator. In the low coupling limit $r \ll 1$ where $h_{n,n+1}^{\text{RWA}}$ scales as $\sqrt{n+1}$, one recovers the familiar Poissonian correlations $g^{(2)}(0) = 1$. On the contrary, at $r = 2$ ($Z_c = 4.1$ k Ω), $h_{1,2}^{\text{RWA}} = 0$ and Eq. (4) yields perfect antibunching of the emitted photons: $g^{(2)}(0) = 0$. In this regime, as illustrated by Fig. 1, a first tunnel event bringing the resonator from Fock state $|0\rangle$ to $|1\rangle$ cannot be followed by a second one as long as the photon has not been emitted in the line.

Standard on-chip microwave resonator designs yield characteristic impedances of the order of 100 Ω , i.e. $r \sim 0.05$. To approach $r \sim 1 - 2$, we have micro-fabricated a resonator with a spiral inductor etched in a 150 nm niobium film sputtered onto a quartz substrate, which was then connected to a SQUID loop acting as a flux-tunable Josephson junction (see Fig. 2). The outgoing radiation was collected in a 50 Ω line through an impedance-matching stage aiming at lowering the resonator quality factor. The geometry of the resonator was optimized using the microwave solver Sonnet, predicting a resonant frequency $\nu_R = 5.1$ GHz, with a characteristic impedance of 2.05 k Ω , corresponding to $r = 1.0$, and a quality factor $Q = 2\pi\nu_r/\kappa = 42$ [31]. The actual values measured using the calibration detailed below are $\nu_r = 4.4$ GHz, $Q = 36.6$, and a characteristic impedance $Z_c = 1.97 \pm 0.06$ k Ω , corresponding to a coupling parameter $r = 0.96 \pm 0.03$, and thus to an expected $E_J^*/E_J = 0.62 \pm 0.01$. We attribute the small difference between design and experimental values to a possible under-estimation in our microwave simulations of the capacitive coupling of the resonator to the surrounding grounding box.

The sample is placed in a shielded sample holder thermally anchored to the mixing chamber of a dilution refrigerator at $T = 12$ mK. As shown in Fig. 2, the sample is connected to a bias tee, with a dc port connected to a filtered voltage divider, and a rf port connected to a hybrid coupler acting as a microwave beam splitter towards two amplified lines with an effective noise temperature of 13.8 K. After bandpass filtering at room temperature, the signals in these two channels are down converted to the 0 - 625 MHz frequency range using two mixers sharing the same local oscillator at $\nu_{\text{LO}} = 4.71$ GHz, above the resonator frequency. The output signals are then digitized at 1.25 GSamples/s and all the relevant correlation functions are computed numerically.

To calibrate in-situ the gain G of the detection chain and the impedance $Z(\nu)$ seen by the junction, we measure the power emitted by the junction in two different regimes. First, we bias the junction well above the gap

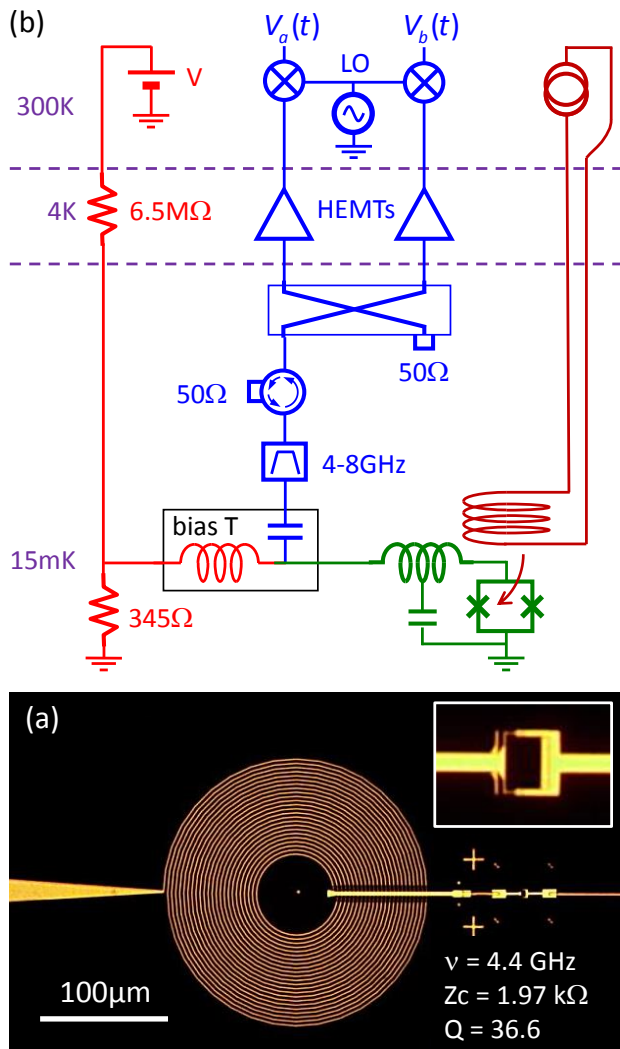


FIG. 2: **Experimental setup.** (a) Optical micrograph of the sample showing the Al/AIO_x/Al SQUID (inset) implementing the Josephson junction and the resonator made of a Nb spiral inductor with stray capacitance to ground. (b) Schematics of the circuit showing the sample (green), the coil circuit for tuning the Josephson energy (brown), the dc bias line (red), and the bias tee connected to the microwave line (blue) with bandpass filters, isolators, and a symmetric splitter connected to two identical measuring lines with amplifiers at 4.2 K and demodulators at room temperature [31].

voltage $V_{\text{gap}} = 210 \mu\text{V}$ and measure the voltage derivative of the quasiparticle shot noise power spectral density, equal to $2eR_t \text{Re}Z(\nu)/|R_t + Z(\nu)|^2$ with $R_t = 222 \pm 3 \text{ k}\Omega$ the normal state tunnel resistance of the SQUID measured separately. Second, we sweep the bias voltage V to measure the power at $\nu = h/2eV$ resulting from the inelastic tunneling of Cooper pairs emitting single photons, as given by Eq. (2). The different power dependences on $Z(\nu)$ in these two regimes allows for an absolute determination of G and $Z(\nu)$ [31], the latter being shown in red in Fig. 3b.

In Fig. 3a, the measured 2D emission map as a function of bias voltage and frequency shows the single photon regime along the diagonal. A cut at the resonator frequency (blue line in Fig. 3b) reveals an emission width of 2.9 MHz, which we attribute to low frequency fluctuations of the bias voltage that are mostly of thermal origin. On the 2D emission map, two faint lines (pointed by the oblique yellow arrows) also appear at $2eV = h(\nu \pm \nu_P)$, and correspond to the simultaneous emission of a photon in the resonator and the emission/absorption of a photon in a parasitic resonance of the detection line at $\nu_P = 325 \text{ MHz}$. Comparing the weight of these peaks to the main peak at $2eV = h\nu$ yields a 61Ω characteristic impedance of the parasitic mode and a 15 mK mode temperature in good agreement with the refrigerator temperature.

We now set the bias at $V = h\nu_r/2e = 9.1 \mu\text{V}$, so that each Cooper pair tunneling through the junction emits one photon at the resonance frequency, and we detect the signals leaking out of the resonator in a frequency

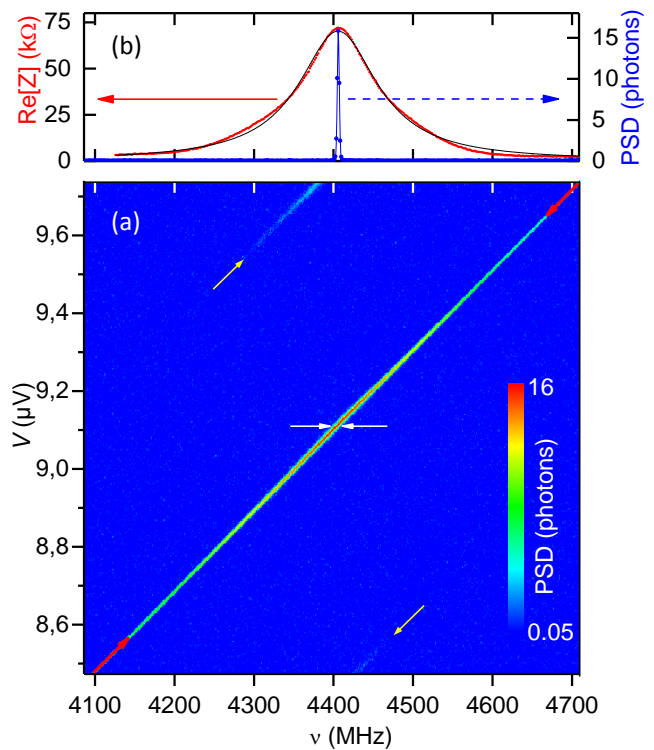


FIG. 3: **Emitted microwave power and impedance seen by the junction.** (a) 2D map of the emitted power spectral density (PSD) as a function of the frequency ν and bias voltage V , expressed in photon occupation number (logarithmic color-scale). (b) Spectral line at $V = 9.11 \mu\text{V}$ (blue points) obtained from a cut in the 2D map along the horizontal white arrows and real part of the impedance $\text{Re}[Z(\nu)]$ seen by the SQUID (red points). The corresponding solid blue and black lines are a Gaussian fit with 2.9 MHz FWHM and a Lorentzian fit with 120 MHz FWHM.

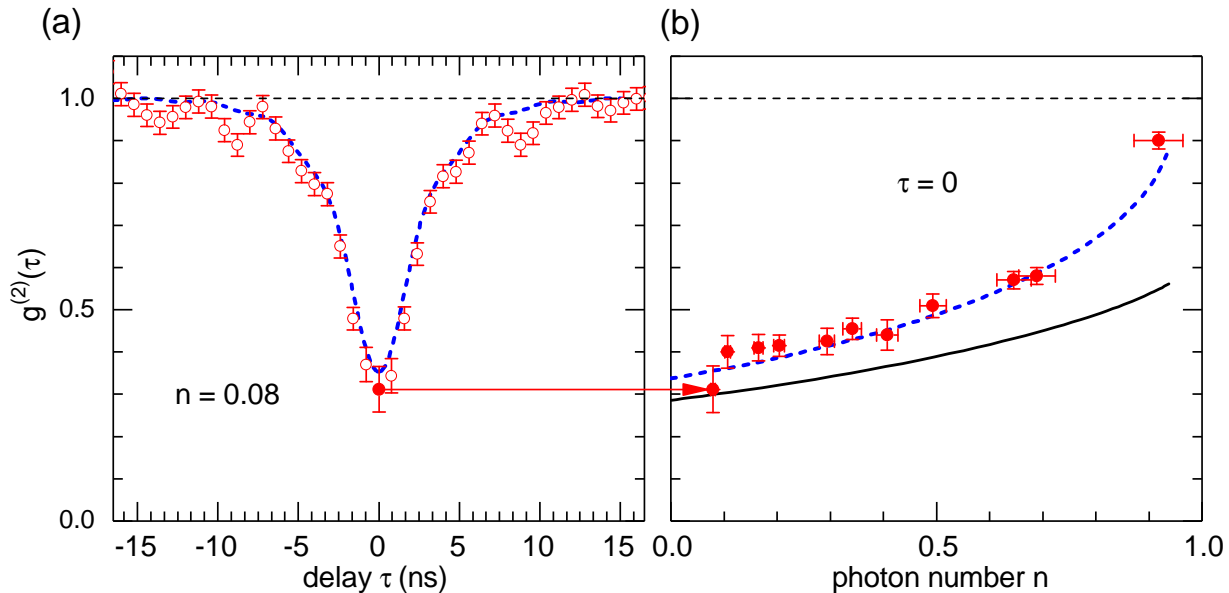


FIG. 4: **Antibunching of the emitted radiation** at bias $V = h\nu_R/2e = 9.11 \mu\text{V}$. **(a)** Measured (dots) and theoretically predicted (dashed line) second order correlation function $g^{(2)}$ as a function of delay τ for $n = 0.08$ photons in the resonator. Error bars indicate \pm the measured statistical standard deviation; note that it is twice as big at $\tau = 0$ because of the delta-correlated thermal noise of the amplifiers. **(b)** Experimental (dots) and theoretical (dashed line) $g^{(2)}(0)$ as a function of n . The solid line would be the theoretical prediction without taking into account the finite bandwidth of our detection chain.

band of 525 MHz (~ 4.4 resonator's FWHM) centered at ν_R . This apparently large detection window – 180 times wider than the emission line, see Fig. 3b – is actually barely enough to measure the fast fluctuations occurring at frequencies up to the inverse resonator lifetime. An even larger bandwidth would bring the measured $g^{(2)}$ closer to the expected value of Eq. (4) but would also increase the parasitic fluctuations due to amplifiers' noise and increase the necessary averaging time. Our choice is thus a compromise, leading to a 15-day long averaging for the lowest occupation number. As we split the signal right out of the sample before sending it to two independent amplification chains a and b (Fig. 2), we can use a Hanbury Brown-Twiss scheme to measure $g^{(2)}(\tau)$ by two different methods. First, we obtain

$$g^{(2)}(\tau) = \frac{\langle P_a(t)P_b(t+\tau) \rangle}{\langle P_a(t) \rangle \langle P_b(t+\tau) \rangle} \quad (5)$$

from the cross-correlations of the instantaneous powers $P_a(t), P_b(t)$ measured at the end of the chains. In practice, the sample's weak contribution has not been extracted from the large background noise of the amplifiers, which we measure by setting the bias voltage to zero. To overcome this complication and get a better precision on $g^{(2)}$, we also took an alternative approach built on a method of Ref. [35]: instead of detecting microwave powers, we heterodyne the signals $V_a(t), V_b(t)$ (Fig. 2) to measure their two quadratures and rebuild their complex envelopes $S_a(t), S_b(t)$ [31]. After compensation of

the delay between the two lines, we compute the complex cross-signal $C(t) = S_a^*(t)S_b(t)$, which is proportional to the power emitted by the resonator and has a background contribution that averages to a much smaller value. The instantaneous noise on $C(t)$ is also spread evenly between real and imaginary parts and is then $\sqrt{2}$ smaller than the noise on $P_a(t)$ and $P_b(t)$. $g^{(2)}(\tau)$ can then be extracted from the correlation function of $C(t)$ and $C^*(t)$ [31].

Both methods gave the same results within their standard deviations, and the $g^{(2)}$ values shown in Fig. 4 correspond to the average of the two procedures. As we decrease the photon emission rate by adjusting E_J with the magnetic flux threading the SQUID, $g^{(2)}(0)$ decreases. For the lowest measured emission rate of 60 millions photons per second, corresponding to an average resonator population of 0.08 photons, $g^{(2)}(0)$ goes down to 0.31 ± 0.04 , in good agreement with the theoretical prediction of 0.27, cf. Eq. (4) for $r=0.96$. This is the main result of this work, which demonstrates a significant antibunching of the emitted photons. In agreement with Eq. (4), the characteristic time scale of the $g_2(\tau)$ variations coincides with the 1.33 ns resonator lifetime deduced from the calibrations. As our design did not reach $r = 2$, the transition from $|1\rangle$ to $|2\rangle$ is not completely forbidden, and from then on, transitions from $|2\rangle$ to $|3\rangle$ and higher Fock states can occur. The larger E_J , the more likely to have 2 photons and hence photon bunching. To predict the time-dependent $g^{(2)}(\tau)$ for arbitrary E_J , we

solve the full quantum master equation

$$\dot{\rho} = -\frac{i}{\hbar}[H^{\text{RWA}}, \rho] + \frac{\kappa}{2}(2a\rho a^\dagger - a^\dagger a\rho - \rho a^\dagger a). \quad (6)$$

This approach also allows for the quantitative modeling of the experimental measurement via a four-time correlator [31]. Properly accounting for filtering in the measurement chain (see Ref. [3, 35] and Supplemental Material [31]), this description accurately reproduces the experimental results in Fig. 4 (lines) without any fitting parameters.

We finally probe the renormalization of E_J by the zero point fluctuations of the resonator using Eq. (2). This requires to maintain the resonator photon population much below 1, which should be obtained by reducing the Josephson energy using the flux through the SQUID. However, magnetic hysteresis due to vortex pinning in the nearby superconducting electrodes prevented us from ascribing a precise flux to a given applied magnetic field, the only straightforward and reliable working point at our disposal thus occurring at zero magnetic flux and maximum Josephson energy. To ensure that the SQUID remains in the DCB regime even at this maximum E_J , and ensure a low enough photon population, we select a bias voltage $V = 10.15 \mu\text{V}$ yielding radiation at 4.91 GHz, far off the resonator frequency. Here again, the normal current shot noise is used as a calibrated noise source to measure in-situ $G\text{Re}Z(\nu = 4.91 \text{ GHz})$. The effective Josephson energy $E_J^* = 1.86 \mu\text{eV}$ extracted in this way is significantly smaller than the Ambegaokar-Baratoff value of $E_J = 3.1 \mu\text{eV}$, and in good agreement with our prediction of $E_J^* = 1.92 \pm 0.02 \mu\text{eV}$ [36].

In conclusion, we have explored a new regime of the quantum electrodynamics of coherent conductors by strongly coupling a dc biased Josephson junction to its electromagnetic environment, a high-impedance microwave resonator. This enhanced coupling first results in a sizeable renormalization of the effective Josephson energy of the junction. Second, it provides an extremely simple and bright source of antibunched photons. Appropriate time shaping either of the bias voltage [37], or the resonator frequency, or the Josephson energy [38] should allow for on-demand single photon emission. This new regime that couples quantum electrical transport to quantum electromagnetic radiation opens the way to new devices for quantum microwaves generation. It also allows many fundamental experiments like investigating high photon number processes, parametric transitions in the strong coupling regime [20, 21, 39, 40], the stabilization of a Fock state by dissipation engineering [37], or the development of new type of Qbit based on the Lamb-shift induced by the junction [41].

We thank B. Huard, S. Seidelin, P. Milman and M. Hofheinz for useful discussions, and gratefully acknowledge partial support from LabEx PALM (ANR-10-LABX-0039-PALM), ANR contracts ANPhoTeQ and

GEARED, from the ANR-DFG Grant JosephCharli, and from the ERC through the NSECROBE grant, from IQST and the German Science Foundation (DFG) through AN336/11-1. S.D. acknowledges financial support from the Carl-Zeiss-Stiftung.

* These two authors contributed equally.

† Electronic address: email: joachim.ankerhold@uni-ulm.de

‡ Electronic address: email: fabien.portier@cea.fr

- [1] Z.-L. Xiang, M. Zhang, L. Jiang, and P. Rabl, *Phys. Rev. X* **7**, 011035 (2017), URL <https://link.aps.org/doi/10.1103/PhysRevX.7.011035>.
- [2] A. A. Houck, D. I. Schuster, J. M. Gambetta, J. A. Schreier, B. R. Johnson, J. M. Chow, L. Frunzio, J. Majer, M. H. Devoret, S. M. Girvin, et al., *Nature* **449**, 328 (2007).
- [3] D. Bozyigit, C. Lang, L. Steffen, J. M. Fink, C. Eichler, M. Baur, R. Bianchetti, P. J. Leek, S. Filipp, M. P. da Silva, et al., *Nat Phys* **7**, 154 (2011), ISSN 1745-2473, URL <http://dx.doi.org/10.1038/nphys1845>.
- [4] A. Cottet, T. Kontos, and B. Douçot, *Phys. Rev. B* **91**, 205417 (2015), URL <https://link.aps.org/doi/10.1103/PhysRevB.91.205417>.
- [5] O. Dmytruk, M. Trif, C. Mora, and P. Simon, *Phys. Rev. B* **93**, 075425 (2016), URL <https://link.aps.org/doi/10.1103/PhysRevB.93.075425>.
- [6] C. Mora, C. Altimiras, P. Joyez, and F. Portier, *Phys. Rev. B* **95**, 125311 (2017), URL <https://link.aps.org/doi/10.1103/PhysRevB.95.125311>.
- [7] C. Altimiras, F. Portier, and P. Joyez, *Phys. Rev. X* **6**, 031002 (2016), URL <https://link.aps.org/doi/10.1103/PhysRevX.6.031002>.
- [8] A. L. Grimsmo, F. Qassemi, B. Reulet, and A. Blais, *Phys. Rev. Lett.* **116**, 043602 (2016), URL <https://link.aps.org/doi/10.1103/PhysRevLett.116.043602>.
- [9] J. Leppäkangas, G. Johansson, M. Marthaler, and M. Fogelström, *New Journal of Physics* **16**, 015015 (2014), URL <http://stacks.iop.org/1367-2630/16/i=1/a=015015>.
- [10] J. Leppäkangas, G. Johansson, M. Marthaler, and M. Fogelström, *Phys. Rev. Lett.* **110**, 267004 (2013), URL <http://link.aps.org/doi/10.1103/PhysRevLett.110.267004>.
- [11] Y.-Y. Liu, K. Petersson, J. Stehlik, J. Taylor, and J. Petta, *Phys. Rev. Lett.* **113**, 036801 (2014), URL <http://link.aps.org/doi/10.1103/PhysRevLett.113.036801>.
- [12] J.-C. Forgues, C. Lupien, and B. Reulet, *Phys. Rev. Lett.* **114**, 130403 (2015), URL <https://link.aps.org/doi/10.1103/PhysRevLett.114.130403>.
- [13] F. Chen, J. Li, A. D. Armour, E. Brahim, J. Stettenheim, A. J. Sirois, R. W. Simmonds, M. P. Blencowe, and A. J. Rimberg, *Phys. Rev. B* **90**, 020506 (2014), URL <http://link.aps.org/doi/10.1103/PhysRevB.90.020506>.
- [14] M. C. Cassidy, A. Bruno, S. Rubbert, M. Irfan, J. Kammhuber, R. N. Schouten, A. R. Akhmerov, and L. P. Kouwenhoven, *Science* **355**, 939 (2017), ISSN 0036-8075,

- <http://science.sciencemag.org/content/355/6328/939.full.pdf>[33]
 URL <http://science.sciencemag.org/content/355/6328/939>.
- [15] J.-C. Forgues, C. Lupien, and B. Reulet, *Phys. Rev. Lett.* **113**, 043602 (2014), URL <http://link.aps.org/doi/10.1103/PhysRevLett.113.043602>.
- [16] M. J. Gullans, J. Stehlik, Y.-Y. Liu, C. Eichler, J. R. Petta, and J. M. Taylor, *Phys. Rev. Lett.* **117**, 056801 (2016), URL <http://link.aps.org/doi/10.1103/PhysRevLett.117.056801>.
- [17] M. Westig, B. Kubala, O. Parlavecchio, Y. Mukharsky, C. Altimiras, P. Joyez, D. Vion, P. Roche, D. Esteve, M. Hofheinz, et al., *Phys. Rev. Lett.* **119**, 137001 (2017), URL <https://link.aps.org/doi/10.1103/PhysRevLett.119.137001>.
- [18] S. Jebari, F. Blanchet, A. Grimm, D. Hazra, R. Albert, P. Joyez, D. Vion, D. Esteve, F. Portier, and M. Hofheinz, *Nature Electronics* **1**, 223 (2018), URL <https://doi.org/10.1038/s41928-018-0055-7>.
- [19] M. Hofheinz, F. Portier, Q. Baudouin, P. Joyez, D. Vion, P. Bertet, P. Roche, and D. Esteve, *Phys. Rev. Lett.* **106**, 217005 (2011), URL <http://link.aps.org/doi/10.1103/PhysRevLett.106.217005>.
- [20] V. Gramich, B. Kubala, S. Rohrer, and J. Ankerhold, *Phys. Rev. Lett.* **111**, 247002 (2013), URL <http://link.aps.org/doi/10.1103/PhysRevLett.111.247002>.
- [21] S. Dambach, B. Kubala, V. Gramich, and J. Ankerhold, *Phys. Rev. B* **92**, 054508 (2015), URL <https://link.aps.org/doi/10.1103/PhysRevB.92.054508>.
- [22] J. P. Martinez, S. Leger, N. Gheeraert, R. Dassonneville, L. Planat, F. Foroughi, Y. Krupko, O. Buisson, C. Naud, W. Guichard, et al., *A tunable josephson platform to explore many-body quantum optics in circuit-qed* (2018), arXiv:1802.00633.
- [23] R. Kuzmin, R. Mencia, N. Grabon, N. Mehta, Y.-H. Lin, and V. E. Manucharyan, *Quantum electrodynamics of a superconductor-insulator phase transition* (2018), arXiv:1805.07379.
- [24] K. Le Hur, *Phys. Rev. B* **85**, 140506 (2012), URL <https://link.aps.org/doi/10.1103/PhysRevB.85.140506>.
- [25] M. Goldstein, M. H. Devoret, M. Houzet, and L. I. Glazman, *Phys. Rev. Lett.* **110**, 017002 (2013), URL <https://link.aps.org/doi/10.1103/PhysRevLett.110.017002>.
- [26] B. Peropadre, D. Zueco, D. Porras, and J. J. García-Ripoll, *Phys. Rev. Lett.* **111**, 243602 (2013), URL <https://link.aps.org/doi/10.1103/PhysRevLett.111.243602>.
- [27] N. Gheeraert, S. Bera, and S. Florens, *New Journal of Physics* **19**, 023036 (2017), URL <http://stacks.iop.org/1367-2630/19/i=2/a=023036>.
- [28] G.-L. Ingold and Y. V. Nazarov, in *Single charge tunneling*, edited by H. Grabert and M. H. Devoret (Plenum, 1992).
- [29] D. Averin, Y. Nazarov, and A. Odintsov, *Physica B* **165–166**, 945 (1990).
- [30] T. Holst, D. Esteve, C. Urbina, and M. H. Devoret, *Phys. Rev. Lett.* **73**, 3455 (1994).
- [31] More details about the fabrication process and measurement procedure can be found in the on-line Supplementary Material.
- [32] G. Schn and A. Zaikin, *Physics Reports* **198**, 237 (1990), ISSN 0370-1573, URL <http://www.sciencedirect.com/science/article/pii/037015739090156V>.
- [33] H. Grabert, G.-L. Ingold, and B. Paul, *EPL (Europhysics Letters)* **44**, 360 (1998), URL <http://stacks.iop.org/0295-5075/44/i=3/a=360>.
- [34] P. Joyez, *Phys. Rev. Lett.* **110**, 217003 (2013), URL <https://link.aps.org/doi/10.1103/PhysRevLett.110.217003>.
- [35] M. P. da Silva, D. Bozyigit, A. Wallraff, and A. Blais, *Phys. Rev. A* **82**, 043804 (2010), URL <https://link.aps.org/doi/10.1103/PhysRevA.82.043804>.
- [36] The flux jumps due to vortex depinning were slow enough that we could compensate for them manually. We could thus obtain the total flux dependence of the emitted power, whose fit with a sinusoidal law yields the same value for E_J within experimental errors and a negligible asymmetry.
- [37] J.-R. Souquet and A. A. Clerk, *Phys. Rev. A* **93**, 060301 (2016), URL <https://link.aps.org/doi/10.1103/PhysRevA.93.060301>.
- [38] A. Grimm, F. Blanchet, R. Albert, J. Leppkangas, S. Jebari, D. Hazra, F. Gustavo, J.-L. Thomassin, E. Dupont-Ferrier, F. Portier, et al., *A bright on-demand source of anti-bunched microwave photons based on inelastic cooper pair tunneling* (2018), arXiv:1804.10596.
- [39] C. Padurariu, F. Hassler, and Y. V. Nazarov, *Phys. Rev. B* **86**, 054514 (2012), URL <https://link.aps.org/doi/10.1103/PhysRevB.86.054514>.
- [40] S. Meister, M. Mecklenburg, V. Gramich, J. T. Stockburger, J. Ankerhold, and B. Kubala, *Phys. Rev. B* **92**, 174532 (2015), URL <https://link.aps.org/doi/10.1103/PhysRevB.92.174532>.
- [41] J. Estève, M. Aprili, and J. Gabelli, arXiv:1807.02364 (2018).
- [42] B. Kubala, V. Gramich, and J. Ankerhold, *Phys. Scr.* **T165**, 014029 (2015), URL <http://stacks.iop.org/1402-4896/2015/i=T165/a=014029>.
- [43] A. D. Armour, B. Kubala, and J. Ankerhold, *Phys. Rev. B* **96**, 214509 (2017), URL <https://link.aps.org/doi/10.1103/PhysRevB.96.214509>.
- [44] D. Walls and G. Milburn, *Quantum Optics* (Springer Berlin Heidelberg, 2009), ISBN 9783540814887.
- [45] S. Boutin, D. M. Toyli, A. V. Venkatramani, A. W. Eddins, I. Siddiqi, and A. Blais, *Phys. Rev. Applied* **8**, 054030 (2017), URL <https://link.aps.org/doi/10.1103/PhysRevApplied.8.054030>.
- [46] E. del Valle, A. Gonzalez-Tudela, F. P. Laussy, C. Tejedor, and M. J. Hartmann, *Phys. Rev. Lett.* **109**, 183601 (2012), URL <https://link.aps.org/doi/10.1103/PhysRevLett.109.183601>.
- [47] E. del Valle, *New Journal of Physics* **15**, 025019 (2013), URL <http://stacks.iop.org/1367-2630/15/i=2/a=025019>.
- [48] C. Dory, K. A. Fischer, K. Müller, K. G. Lagoudakis, T. Sarmiento, A. Rundquist, J. L. Zhang, Y. Ke-laita, N. V. Saprà, and J. Vučković, *Phys. Rev. A* **95**, 023804 (2017), URL <https://link.aps.org/doi/10.1103/PhysRevA.95.023804>.
- [49] C. M. Caves, *Phys. Rev. D* **26**, 1817 (1982).
- [50] D. Bozyigit, C. Lang, L. Steffen, J. M. Fink, C. Eichler, M. Baur, R. Bianchetti, P. J. Leek, S. Filipp, M. P. da Silva, et al., *Nat Phys* **7**, 154 (2011).
- [51] D. F. Walls and G. J. Milburn, *Quantum optics* (Springer, 2008), 2nd ed.
- [52] J. M. Fink, M. Kalaei, A. Pitanti, R. Norte, L. Heinzele, M. Davanço, K. Srinivasan, and O. Painter, *Nature* **500**, 207 (2016), URL <https://doi.org/10.1038/nature16176>.

- ture Communications **7**, 12396 EP (2016), article, URL <http://dx.doi.org/10.1038/ncomms12396>.
- [53] M.-C. Harabula, T. Hasler, G. Fülöp, M. Jung, V. Ranjan, and C. Schönenberger, Phys. Rev. Applied **8**, 054006 (2017), URL <https://link.aps.org/doi/10.1103/PhysRevApplied.8.054006>.
- [54] T. Hasler, M. Jung, V. Ranjan, G. Puebla-Hellmann, A. Wallraff, and C. Schönenberger, Phys. Rev. Applied **4**, 054002 (2015), URL <https://link.aps.org/doi/10.1103/PhysRevApplied.4.054002>.
- [55] C. Altimiras, O. Parlavecchio, P. Joyez, D. Vion, P. Roche, D. Esteve, and F. Portier, Applied Physics Letters **103**, 212601 (2013), <https://doi.org/10.1063/1.4832074>, URL <https://doi.org/10.1063/1.4832074>.
- [56] T. Holmqvist, M. Meschke, and J. P. Pekola, Journal of Vacuum Science & Technology B: Microelectronics and Nanometer Structures Processing, Measurement, and Phenomena **26**, 28 (2008), <https://avs.scitation.org/doi/pdf/10.1116/1.2817629>, URL <https://avs.scitation.org/doi/abs/10.1116/1.2817629>.
- [57] I. Wolff, *Coplanar Microwave Integrated Circuits* (Wiley, 2006).
- [58] G. J. Dolan, Applied Physics Letters **31**, 337 (1977), <https://doi.org/10.1063/1.89690>, URL <https://doi.org/10.1063/1.89690>.

Antibunched photons emitted by a dc-biased Josephson junction: Supplemental material

DERIVATION OF EQ. 2 OF THE MAIN TEXT USING $P(E)$ THEORY

The spectral density of the emitted radiation is given by [19]:

$$\gamma(V, \nu) = \frac{2\text{Re}[Z(\nu)]}{R_Q} \frac{\pi}{2\hbar} E_J^2 P(2eV - h\nu), \quad (\text{S1})$$

where $Z(\nu)$ is the impedance across the junction, R_Q is the superconducting resistance quantum $R_Q = h/4e^2$, E_J is the Josephson energy of the junction, and $P(E)$ represents the probability density for a Cooper pair tunneling across the junction to dissipate the energy E into the electromagnetic environment described by $Z(\nu)$ [28]. $P(E)$ is a highly nonlinear transform of $Z(\nu)$:

$$\begin{aligned} P(E) &= \frac{1}{2\pi\hbar} \int_{-\infty}^{\infty} \exp[J(t) + iEt/\hbar] dt \\ J(t) &= \int_{-\infty}^{+\infty} \frac{d\omega}{\omega} \frac{2\text{Re}Z(\omega)}{R_Q} \frac{e^{-i\omega t} - 1}{1 - e^{-\beta\hbar\omega}}, \end{aligned} \quad (\text{S2})$$

where $\beta = 1/k_B T$. For an LC oscillator of infinite quality factor at zero temperature, $P(E)$ is given by

$$P(E) = e^{-r} \sum_n \frac{r^n}{n!} \delta(eV - n\hbar\omega_0) \quad (\text{S3})$$

where $r = \pi\sqrt{\frac{L}{C}}/R_Q$ and $\omega_0 = 1/\sqrt{LC}$.

Here, we consider the case of a mode of finite linewidth, so that near the resonance the real part of the impedance can be approximated as

$$\frac{2\text{Re}Z(\omega)}{R_Q} \simeq r\mathcal{L}(\omega, \omega_0, Q). \quad (\text{S4})$$

where

$$\mathcal{L}(\omega, \omega_0, Q) \equiv \frac{2}{\pi} \frac{Q}{1 + 4Q^2 \left(\frac{\omega}{\omega_0} - 1\right)^2}$$

denotes a Lorentzian function centered at ω_0 with a maximum value $\frac{2}{\pi}Q$ and a quality factor $Q = \frac{\omega_0}{\Delta\omega}$. Note that $\int \mathcal{L}(\omega, \omega_0, Q) d\omega = \omega_0$.

For such a finite- Q mode, we aim to get a formula similar to Eq. S3, i.e. we look for an expansion

$$P(E) = P_0(E) + P_1(E) + P_2(E) + \dots + P_n(E) + \dots \quad (\text{S5})$$

where each $P_n(E) \propto r^n$. However, from the integral expressions (S2), accessing the different multiphoton peaks, i.e. calculating $P(E \simeq n\hbar\omega_0)$ is not straight-forward. Such an expansion can be obtained using the so-called Minnhagen equation [28], which is an exact integral relation obeyed by $P(E)$, valid for any impedance. We first establish the Minnhagen equation starting from

$$e^{J(t)} - e^{J(\infty)} = \int_{-\infty}^t d\tau J'(\tau) e^{J(\tau)},$$

which, using the definition (S2) of J can be recast as

$$e^{J(t)} - e^{J(\infty)} = -i \int_{-\infty}^{+\infty} d\omega' h(\omega') \int_{-\infty}^{\infty} d\tau e^{-i\omega'\tau} e^{J(\tau)} \theta(t - \tau)$$

where θ is the Heaviside function, $h(\omega) = \frac{1}{1-e^{-\beta\hbar\omega}} \frac{2\text{Re}Z(\omega)}{R_Q}$ and using the fact that $J(-\infty) = J(\infty)$. The rightmost integral being the Fourier transform of a product, we replace it by the convolution product of the Fourier transforms and use the detailed balance property of h and P to simplify the r.h.s.:

$$\begin{aligned} e^{J(t)} - e^{J(\infty)} &= -i \int_{-\infty}^{+\infty} d\omega' h(\omega') \int du \left(\pi\delta(u) + \frac{ie^{it'u}}{u} \right) P(-\omega' - u) \\ &= \int_{-\infty}^{+\infty} d\omega' h(\omega') \int du \frac{e^{itu}}{u} P(-\omega' - u). \end{aligned}$$

Finally, we take the Fourier transform on both sides and rearrange, which yields the Minnhagen equation

$$P(E) = \frac{\hbar}{E} \int P(E - \hbar\omega) \frac{1}{1-e^{-\beta\hbar\omega}} \frac{2\text{Re}Z(\omega)}{R_Q} d\omega + \delta(E) e^{\text{Re}J(\infty)}. \quad (\text{S6})$$

At zero temperature $\frac{1}{1-e^{-\beta\hbar\omega}} \rightarrow \theta(\omega)$ and $P(E)$ is zero for negative energies, so that the Minnhagen equation is most frequently found written as

$$P(E) = \frac{\hbar}{E} \int_0^E P(E - \hbar\omega) \frac{2\text{Re}Z(\omega)}{R_Q} d\omega + \delta(E) e^{\text{Re}J(\infty)}. \quad (\text{S7})$$

Plugging the expansion (S5) into Eq. S6, one immediately gets

$$\begin{aligned} P_0(E) &= \delta(E) e^{J(\infty)} \\ P_1(E) &= \frac{1}{E} \int_{-\infty}^{\infty} P_0(E - \hbar\omega) \frac{r\mathcal{L}(\omega, \omega_0, Q)}{1 - e^{-\beta\hbar\omega}} d\hbar\omega \\ &\simeq \frac{e^{J(\infty)}}{\hbar\omega_0} r\mathcal{L}\left(\frac{E}{\hbar}, \omega_0, Q\right) \end{aligned}$$

where the approximation of the last line was obtained assuming that $k_B T \ll \hbar\omega_0$ and taking the value of the denominator at $E = \hbar\omega_0$ –where \mathcal{L} (and P_1) peak– which is reasonable if the Q is large enough. By repeated replacement in Eq. S6 and with similar approximations, one systematically obtains the higher orders terms of (S5) as shifted Lorentzians of constant Q

$$P_{n \geq 1}(E) \simeq e^{J(\infty)} \frac{r^n}{nn!} \frac{\mathcal{L}(E/\hbar, n\omega_0, Q)}{\hbar\omega_0}$$

whose value at each peak are

$$P_{n \geq 1}(E = n\hbar\omega_0) = \frac{2}{\pi} e^{J(\infty)} \frac{r^n}{nn!} \frac{Q}{\hbar\omega_0}$$

yielding a tunneling rate at the peaks

$$\Gamma_{2e}(eV = n\hbar\omega_0) = \frac{1}{\hbar} \frac{E_J^2 e^{J(\infty)}}{\hbar\omega_0} \frac{r^n}{n!} \frac{Q}{n}.$$

Note that the Cooper pair rates at different orders scale with an extra Q/n compared to the naive rates obtained from Eq. S3.

In the main text, $E_J^2 e^{J(\infty)}$ is called E_J^{*2} . This renormalization of the Josephson energy is obtained from the zero point phase correlator

$$J(\infty) = -\langle \varphi(0)\varphi(0) \rangle = - \int_0^{+\infty} \frac{d\omega}{\omega} \frac{2\text{Re}Z(\omega)}{R_Q} \coth \frac{\beta\omega}{2}$$

which in the limit of $k_B T = 0$ and for an RLC parallel resonator (it is important that $\text{Re}Z(\omega \sim 0) \propto \omega^2$ for proper convergence) yields

$$J(\infty) = - \frac{Qr \left(1 + \frac{2}{\pi} \text{atan} \frac{2Q^2 - 1}{\sqrt{4Q^2 - 1}} \right)}{\sqrt{4Q^2 - 1}} = -r \left(1 - \frac{1}{\pi Q} + \mathcal{O}\left(\frac{1}{Q^2}\right) \right),$$

in agreement with the expression $E_J^* = E_J e^{-r/2}$ used in the main text (The finite- Q correction to this renormalization is of order of 1%, beyond the precision of our measurements). In ref. [19], E_J^{*2} was given with an approximate first-order expansion of the phase correlator valid for small phase fluctuations (and which was correct for the small r value in that paper).

We can use the above expressions to calculate the total emitted power via the single photon processes by two different ways. First, we use Eq. S1 at lowest order, to get the spectral density of the emitted radiation:

$$\gamma(V, \nu) \simeq \frac{2\text{Re}[Z(\nu)]}{R_Q} \frac{\pi}{2\hbar} E_J^2 P_0(E = 2eV - h\nu) = e^{J(\infty)} \frac{2\text{Re}[Z(\nu)]}{R_Q} \frac{\pi}{2\hbar} E_J^2 \delta(2eV - h\nu), \quad (\text{S8})$$

which, upon integrating over ν , gives Eq. 2 of the main text. Alternatively, one can calculate the Cooper pair tunneling rate using P_1 , and get the photon emission rate from energy conservation, yielding the same result.

In Figure S1 we compare the exact $P(E)$ result and the approximate formula, for the experimental parameters.

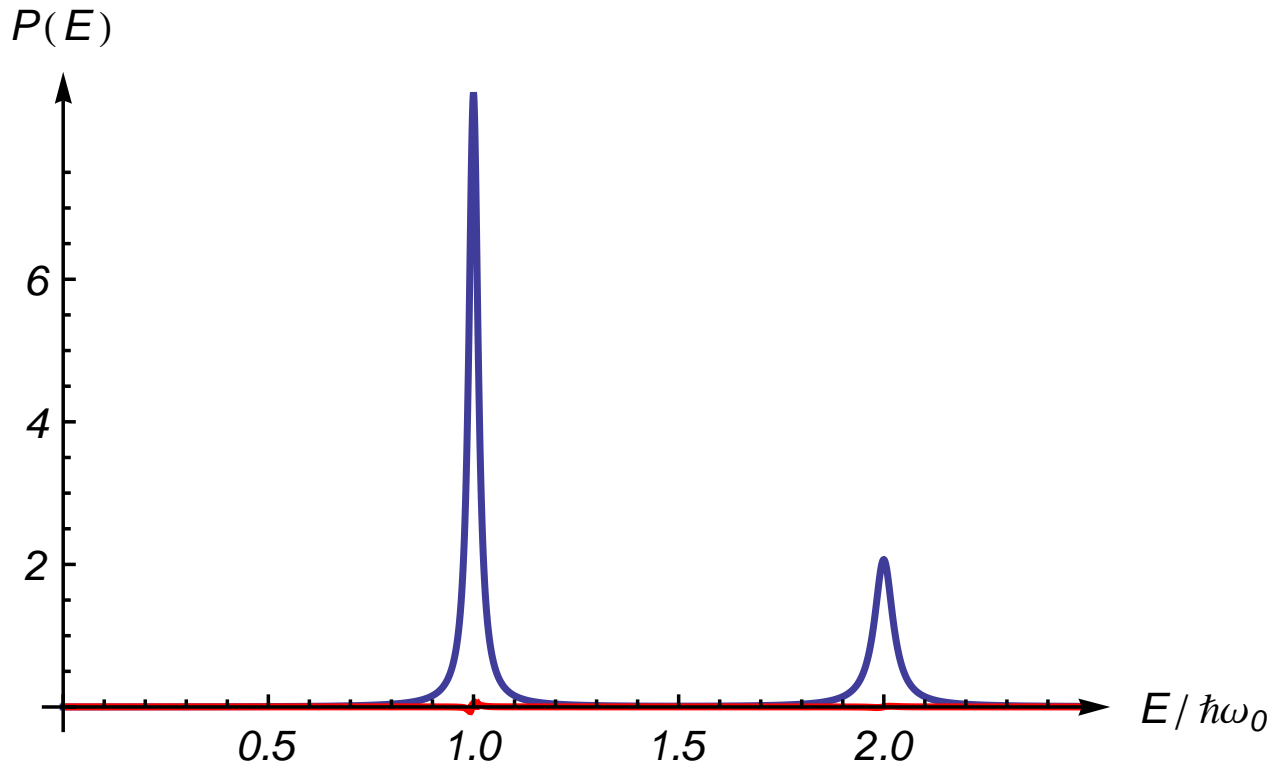


FIG. S1: Comparison the exact $P(E)$ result obtained by numerical evaluation of Eqs. (S2) and the approximate sum of Lorentzians, evaluated for the experimental parameters ($Q = 36.6$, $r = 0.96$). At this scale, the two curves are indistinguishable. The red curve is the difference between the approximate and the exact result.

FRANCK-CONDON BLOCKADE IN THE JOSEPHSON-PHOTONICS HAMILTONIAN

The starting point of our theoretical description, the time-dependent Hamiltonian, see Eq. 1 of the main text,

$$H = (a^\dagger a + 1/2)h\nu_R - E_J(\phi) \cos[2eVt/\hbar - \sqrt{r}(a + a^\dagger)], \quad (\text{S9})$$

describes a *harmonic* oscillator with an unusual, *nonlinear* drive term. Going into a frame rotating with the driving frequency, $\omega_J = 2eV/\hbar$, the oscillator operators, a and a^\dagger , acquire phase terms rotating with the same frequency. The cosine term of the Hamiltonian can then be rewritten in Jacobi-Anger form so that Bessel functions of order k appear as prefactors of terms rotating with integer multiples of the driving frequency, $k\omega_J$.

A rotating-wave approximation neglects time-dependent terms and, taking proper account of the commutation relations of oscillator operators, results in the RWA Hamiltonian (on resonance),

$$H^{\text{RWA}} = iE_J e^{-r/2} : (a^\dagger - a) \frac{J_1(\sqrt{4rn})}{\sqrt{n}} : , \quad (\text{S10})$$

where $: \dots :$ prescribes normal ordering. While the appearance of a Bessel function highlights the nonlinear-dynamical aspects of the system, the Hamiltonian (S10) is completely equivalent to expression Eq. 2 of the main text, given in the main text, using the displacement operator, which emphasizes the connection to Franck-Condon physics.

From either of the two equivalent forms of the RWA Hamiltonian, explicit expressions for the transition matrix elements in terms of associated Laguerre polynomials,

$$h_{n,n+1}^{\text{RWA}} = \frac{ie^{-r/2}\sqrt{r}}{\sqrt{n+1}} L_n^1(r), \quad (\text{S11})$$

can easily be found. Normal ordering reduces the power series of the Bessel function to a low-order polynomial in r (with order n for $h_{n,n+1}^{\text{RWA}}$) and a universal prefactor, describing renormalization of the Josephson coupling. Transition matrix elements thus vanish at the roots of the associated Laguerre polynomials (which in the semiclassical limit of small r and large n approach zeros of the Bessel function J_1).

Some simple results can be directly read off from the transition matrix elements; such as the zero-delay correlations that for weak driving measure the probability of two excitations, $g^{(2)}(0) = \langle n(n-1) \rangle / \langle n \rangle^2 \approx 2P_2/P_1^2 \approx \frac{1}{2} |h_{1,2}^{\text{RWA}}/h_{0,1}^{\text{RWA}}|^2$. The last approximate equality expresses the probabilities $P_{1/2}$ by transition matrix elements, as found by considering the transition rates for the corresponding two-stage excitation process and decay from the Fock states. As mentioned in the main text, in the harmonic limit, $r \ll 1$, where the matrix elements scale with $\sqrt{n+1}$, this would result in the familiar Poissonian correlations and $g^{(2),\text{H0}}(0) = 1$. This contrasts to the antibunching found in our experiment relying on the fact that the experimental parameter $r \sim 1$, while not quite close to the zero of the transition matrix element $h_{1,2}^{\text{RWA}} \propto L_1^1(r) = 2 - r$, is sufficiently large for a considerable suppression of excitations beyond a single photon in the resonator. Coincidentally, the actual value of r is very close to one of the roots, $r \approx 0.93$ of $L_3^1(r) = \frac{1}{6}(-r^3 + 12r^2 - 36r + 24) \propto h_{3,4}^{\text{RWA}}$, so that the system closely resembles a four-level system. In the idealized model description by the approximated Hamiltonian Eq. 3 of the main text and the quantum master equation Eq. 6 of the main text, the vanishing of a transition matrix element implies a strict cut-off of the system's state space at the corresponding excitation level. Various correction terms discussed in the next subsection can lift such a complete blockade and therefore gain relevance once the system is closer to a root than for our $r \sim 1$ value.

CORRECTION TERMS TO HAMILTONIAN AND QUANTUM MASTER EQUATION

The possible impact of various terms and processes not included in RWA Hamiltonian Eq. 3 and quantum master equation Eq. 6 of the main text were carefully checked and found to be completely negligible compared to the error bars due to other experimental uncertainties.

Specifically, the impact of rotating-wave corrections to the time-independent RWA Hamiltonian is sufficiently reduced by the quality factor, $Q = 36.6$. Close to the complete suppression of resonant $g^{(2)}(0)$ contributions at $r = 2$, for very weak driving, and for a bad cavity such processes can become more relevant, as discussed in some detail in Ref. [42]. The limit of extremely strong driving, where $E_J \gtrsim \hbar\nu_R$, not reached here, is discussed in Appendix D of Ref. [43].

Access to higher Fock-states cut-off by vanishing transition matrix elements could, in principle, also be provided by thermal excitations, i.e., by Lindblad terms not included in the $T = 0$ limit of the quantum master equation Eq. 6 of the main text. The latter, however, is safe to use for the experimentally determined mode temperature of ~ 15 mK in our device.

Finally, there are low-frequency fluctuations of the bias voltage, causing the spectral broadening of the emitted radiation (as argued in the main text) that are not accounted for by the quantum master equation Eq. 6 of the main text. Their effect can be modeled, either by an additional Lindblad-dissipator term acting on a density matrix in an extended JJ-resonator space (as described, for instance, in the supplementals to [20]), or by employing the quantum master equation Eq. 6 of the main text and average the results over a (Gaussian) bias-voltage distribution centered around the nominal biasing on resonance.

As argued above, the principal antibunching effect can be understood from transition rate arguments so that it is not sensitive to the phase of the driving, which is becoming undetermined due to the fluctuating voltage bias. In

consequence, the measured $g^{(2)}(0)$ is nearly insensitive to low-frequency fluctuations. Residual effects of detuning on $g^{(2)}(\tau)$ entering $g^{(2)}(0)$ via the filtering are negligible due to the large ratio between inverse resonator lifetime and spectral width, cf. Fig. 3 of the main text.

ACCOUNTING FOR FILTERING

A theoretical approach based on the quantum master equation Eq. 6 of the main text gives direct access to any properly time-/anti-time-ordered products of multiple system operators, which are evaluated by the quantum-regression method. Using input-output theory [44], any arbitrarily ordered product of multiple output operators can readily be expressed in such system-operator objects.

The measured signals, however, do not immediately correspond to output operators but contain operators at the end of the microwave output chain, hence, undergoing additional filtering. An end-of-chain operator acting at a certain time is consequently linked to output operators at all preceding times via a convolution with the filter-response function in the time domain, see the discussion in [35]. Specifically, the measured two-time correlator $G^{(2)}(t_1, t_2) = \langle a_{t_1}^\dagger a_{t_2}^\dagger a_{t_2} a_{t_1} \rangle$, where two operators each are acting at two different times $t_{1/2}$, is related to a four-operator object with each operator acting at a different time.

To simulate the measured $G^{(2)}(t_1, t_2)$, it is necessary to calculate corresponding four-operator objects and then average each instance of time with a probability distribution given by the filter-response function in the time domain. An explicit, worked out example for a three-time object can be found in Appendix E of Ref. [45]. For the special case of a Lorentzian filter-response function a simpler scheme has been put forward [46–48].

For numerical efficiency, here, we calculate the various four-time objects by evaluating the time evolution governed by the exponential of the Liouville superoperator using Sylvester’s formula and Frobenius covariants. This approach is completely equivalent to time-evolving the quantum master equation with any standard differential-equation solver. In a final step, three-dimensional temporal integrals have to be numerically evaluated, wherein the uncertainty of time differences (between points at which the different operators act) is linked to the experimental filter function, see above.

The multiple integrals over differently ordered operator objects hamper an intuitive understanding of the effects of filtering. Therefore, it may be helpful to compare the complex effects of filtering here to a more conventionally encountered scheme describing detection-time uncertainties. In Fig. S2, we show the results of a simple, incomplete filtering description, which only allows for variations in the time difference, $\tau = t_2 - t_1$, but artificially keeps annihilation and creation operators belonging to the same pair at equal times. Apparently, deviations from the correct, complete filtering scheme, cf. Fig. S2, are reasonably small, so that important effects of the filtering are correctly captured; except for the regime of very strong driving, where Rabi-like oscillations in the time-dependence gain strong influence on the measured $g^{(2)}(\tau = 0)$. The simple scheme suggests an intuitive understanding of the effect of filtering as a simple convolution of the unfiltered $G^{(2)}(\tau = t_2 - t_1)$ with the distribution function for the time difference τ due to the filtering effect on $t_{1/2}$. Note, that the time-difference distribution function is itself gained by convoluting the filter function in time domain with itself, so that τ is, in general, not distributed identical to the detection times $t_{1/2}$, but only for special cases of the filtering function.

MEASUREMENT OF THE $g^{(2)}(\tau)$ FUNCTION

Principle of the measurement

Our measurement scheme is to process the small signals leaking out of the sample with standard microwave techniques (filtering, amplification and heterodyning), to digitize them with an acquisition card and to compute numerically the correlation functions relevant to characterize our single-photon source – the most important of them being the second-order coherence function:

$$g^{(2)}(t, \tau) = \frac{\langle \hat{a}^\dagger(t) \hat{a}^\dagger(t + \tau) \hat{a}(t + \tau) \hat{a}(t) \rangle}{\langle \hat{a}^\dagger(t) \hat{a}(t) \rangle \langle \hat{a}^\dagger(t + \tau) \hat{a}(t + \tau) \rangle}$$

Filtering and amplification are performed in multiple stages but can nonetheless be described as the action of a single effective amplifier of gain G , which adds a noise mode \hbar in a thermal state at temperature T_N to the input signal mode \hat{a} . The output of such an amplifier is then $\sqrt{G}\hat{a} + \sqrt{G-1}\hat{h}^\dagger$ [49].

After digitization of this amplified signal we demodulate numerically its I - Q quadratures. The n -th order moment

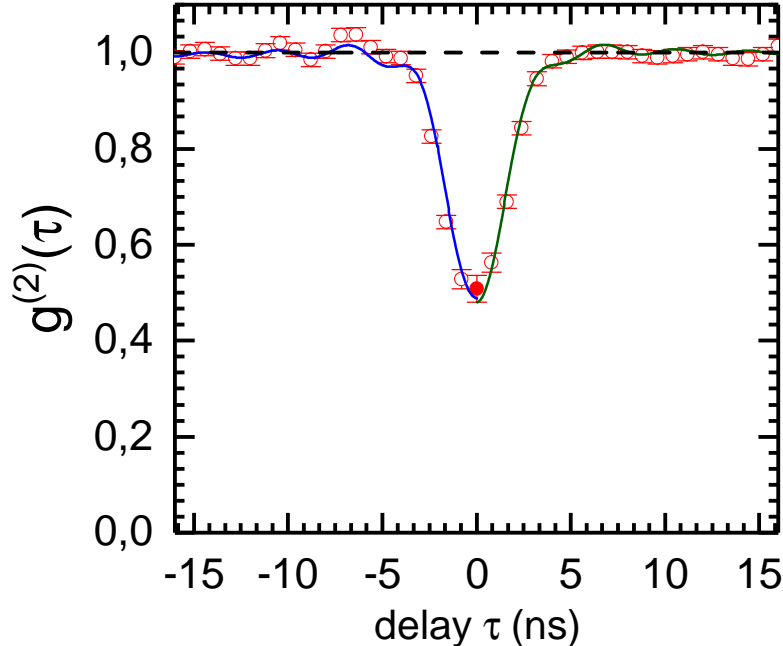


FIG. S2: $g^{(2)}(\tau)$ at $n = 0.5$ photons. The green curve was computed using the 4-point filtering scheme, while the blue curve is the result of a simpler 2-point convolution. For this low photon number, the difference between the two curves is smaller than the error bars on the experimentally measured points (in red).

of the complex envelope $S(t) = I(t) + jQ(t)$ is then a bilinear function of all the moments of \hat{a} and of \hat{h} up to order n [50]. By setting the bias voltage across the emitting squid to zero (the *off* position) and thus putting \hat{a} in the vacuum state, we can measure independently the moments of \hat{h} . We then iteratively subtract them from the moments of S measured when the bias voltage is applied (*on* position) to reconstruct the moments of \hat{a} . Similarly, we can reconstruct $g^{(2)}(\tau)$ from the *on-off* measurements of all the correlation functions of $S(t)$ up to order 4. In addition to this, by splitting the signal from the sample over two detection chains (channels "1" and "2") in a Hanbury Brown-Twiss setup, we can cross-correlate the outputs S_1, S_2 of the two channels to reduce the impact of the added noise on correlation functions. A model of this noise is thus needed to determine which combination of S_1 and S_2 is best suited to measure $g^{(2)}(\tau)$ accurately.

Model for the detection chain

The input-output formalism links the cavity operator \hat{a} to the ingoing and outgoing transmission line operators $\hat{b}_{in}, \hat{b}_{out}$ by: $\sqrt{\kappa}\hat{a}(t) = \hat{b}_{in}(t) + \hat{b}_{out}(t)$, with $\kappa = 2\pi\nu_R/Q$ the energy leak rate of the resonator. In our experimental setup, \hat{b}_{in} describes the thermal radiation coming from the $50\ \Omega$ load on the isolator closest to the sample. This load being thermalized at $15\ \text{mK} \ll h\nu_R/k_B$, the modes impinging onto the resonator can be considered in their ground state and the contribution of \hat{b}_{in} to all the correlation functions vanishes. We thus take \hat{b}_{out} as being an exact image of \hat{a} , and all their normalized correlation functions as being equal.

As described before, the emitted signals are split between two detection chains, filtered, amplified, and mixed with a local oscillator before digitization. Each one of these steps adds a noise mode to the signal (Fig. S3). The beam-splitter right out of the resonator is implemented as a hybrid coupler with a cold $50\ \Omega$ load on its fourth port, which acts as an amplifier of gain $1/2$ and adds a noise mode in the vacuum state \hat{h}_{bs}^\dagger to the signal[51]. The different amplifying stages are summed up into one effective amplifier for each channel, with noise temperatures $T_N^1 = 13.5\ \text{K}$ and $T_N^2 = 14.1\ \text{K}$ respectively. The IQ mixer is used for heterodyning signals, i.e. shifting them to a lower frequency band where we can digitize them, and also adds at least the vacuum level of noise to the signals.

The last step, linear detection of the voltage $V_i(t)$ on channel i by the acquisition card, is harder to model to the quantum level. After digitization, we process chunks of signal of length 1024 samples to compute the analytical signal $S_i(t) = V_i(t) + \mathfrak{H}(V_i(t))$, with \mathfrak{H} the discrete Hilbert transform. As computing the analytical signal from $V_i(t)$ accounts to measuring its two quadratures, which are non-commuting observables, quantum mechanics imposes again an added noise mode. We sum up this digitization noise with the heterodyning noise into a single demodulation noise \hat{h}_{IQ_i} (Fig. S3).

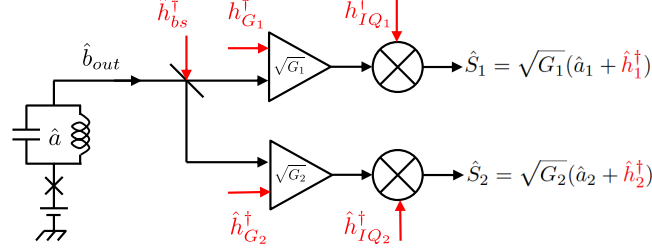


FIG. S3: Detection chain model, taking into account all the added noise modes (in red).

In the end, we record measurements of $\hat{S}_1(t)$ and $\hat{S}_2(t)$, with $\hat{S}_i \propto \hat{a}_i + \hat{h}_i^\dagger$. Here $\hat{a}_i(t) \propto \hat{b}_{out}(t - \tau_i)$, where τ_i is the time delay on channel i . \hat{h}_i is a thermal noise with an occupation number of about 65 photons, which summarizes the noises added by all the detection steps. In practice, the dominant noise contribution stems from the amplifiers closest to the sample. Note also that we do not consider here the effect of the finite bandpass of the filters, which complicates the link between \hat{a}_i and \hat{b}_{out} .

Computing correlations

From each chunk of signal recorded we compute a chunk of $S_i(t)$ of the same length 1024. We then compute the correlation functions we need as:

$$C_{X,Y}(\tau) = \langle X^*(t)Y(t+\tau) \rangle = \mathfrak{F}^{-1}(\mathfrak{F}(X)^* \mathfrak{F}(Y))$$

where $\langle \dots \rangle$ stands for the average over the length of the chunk and \mathfrak{F} is the discrete Fourier transform. Finally, we average the correlation functions from all the chunks and stock this result for further post-processing.

To illustrate how we reconstruct the information on \hat{a} from S_1, S_2 , let's consider the first order coherence function $g^{(1)}(\tau) = \frac{\langle \hat{a}^\dagger(t)\hat{a}(t+\tau) \rangle}{\langle \hat{a}^\dagger \hat{a} \rangle}$. We start with the product:

$$S(t)^* S(t+\tau) \propto \hat{a}^\dagger(t)\hat{a}(t+\tau) + \hat{h}(t)\hat{h}^\dagger(t+\tau) + \hat{a}^\dagger(t)\hat{h}^\dagger(t+\tau) + \hat{h}(t)\hat{a}(t+\tau)$$

We then make the hypothesis that \hat{a} and \hat{h} are independent and hence uncorrelated, which should obviously be the case as the noise in the amplifier cannot be affected by the state of the resonator. Then when averaging:

$$\langle \hat{a}(\tau)\hat{h}(t+\tau) \rangle = \langle \hat{a}(\tau) \rangle \langle \hat{h}(t+\tau) \rangle = 0$$

as there is no phase coherence in the thermal noise, i.e. $\langle \hat{h} \rangle = 0$. We then have:

$$\langle S(t)^* S(t+\tau) \rangle \propto \langle \hat{a}^\dagger(t)\hat{a}(t+\tau) \rangle + \langle \hat{h}(t)\hat{h}^\dagger(t+\tau) \rangle$$

Hence in the *off* position:

$$\langle S(t)^* S(t+\tau) \rangle_{off} \propto \langle \hat{h}(t)\hat{h}^\dagger(t+\tau) \rangle$$

and in the *on* position:

$$\langle S(t)^* S(t+\tau) \rangle_{on} \propto \langle \hat{a}^\dagger(t)\hat{a}(t+\tau) \rangle + \langle S(t)^* S(t+\tau) \rangle_{off}$$

such that:

$$g^{(1)}(\tau) = \frac{\langle S(t)^* S(t+\tau) \rangle_{on} - \langle S(t)^* S(t+\tau) \rangle_{off}}{\langle S^* S \rangle_{on} - \langle S^* S \rangle_{off}}$$

Now as we are considering states of the resonator with at most 1 photon, we typically have:

$$\langle S^* S \rangle_{off} \simeq \langle S^* S \rangle_{on} \gg \langle S^* S \rangle_{on} - \langle S^* S \rangle_{off}$$

Then any small fluctuation of the gain of the detection chain or of the noise temperature during the experiment reduces greatly the contrast on $g^{(1)}(\tau)$. We hence rely on the cross-correlation $X(\tau) = \langle S_1^*(t)S_2(t+\tau) \rangle$. Due to a small cross-talk between the two channels this cross-correlation averages to a finite value even in the *off* position, but which is 60 dB lower than the autocorrelation of each channel. We hence use:

$$g^{(1)}(\tau) = \frac{X(\tau)_{on} - X(\tau)_{off}}{X(0)_{on} - X(0)_{off}}$$

The same treatment allows to compute $g^{(2)}(\tau)$ with slightly more complex calculations. The classical Hanbury Brown-Twiss experiment correlates the signal power over the two channels, i.e. extracts $g^{(2)}(\tau)$ from $\langle S_1^* S_1(t) S_2^* S_2(t+\tau) \rangle$. The *off* value of this correlator is once again much bigger than the relevant information of the *on-off* part, and any drift of the amplifiers blurs the averaged value of $g^{(2)}(\tau)$.

To circumvent this difficulty, we instead use $C(t) = S_1^*(t)S_2(t)$ as a measure of the instantaneous power emitted by the sample, provided that the time delay between the two detection lines is calibrated and compensated for. We then have:

$$g^{(2)}(\tau) = \frac{\langle C(t)C(t+\tau) \rangle_{on} - \langle C(t)C(t+\tau) \rangle_{off}}{(\langle C \rangle_{on} - \langle C \rangle_{off})^2} - 2 \frac{\langle C \rangle_{off}}{\langle C \rangle_{on} - \langle C \rangle_{off}} - \frac{(X(\tau)_{on} - X(\tau)_{off})X(-\tau)_{off}}{(\langle C \rangle_{on} - \langle C \rangle_{off})^2} - \frac{(X(-\tau)_{on} - X(-\tau)_{off})X(\tau)_{off}}{(\langle C \rangle_{on} - \langle C \rangle_{off})^2} \quad (S12)$$

ELECTROMAGNETIC SIMULATIONS

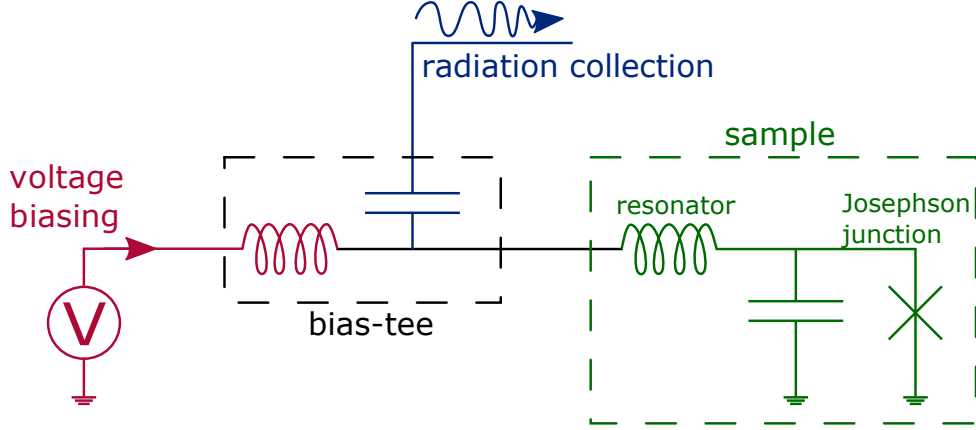


FIG. S4: Schematic diagram of the experiment. The sample, represented by the green box consists in a Josephson junction galvanically coupled to a high impedance resonator consisting in an on-chip spiral inductor. It is connected to a DC biasing circuit, represented in red, and to a 50Ω detection line, represented in blue, through a bias Tee.

The experiment can be schematically represented by figure S4, where the high impedance microwave mode we will use is represented in the green box as a LC resonant circuit. Its resonant pulsation ω_0 and characteristic impedance Z_C are given by

$$Z_C = \sqrt{\frac{L}{C}} \quad ; \quad \omega_0 = \frac{1}{\sqrt{LC}}.$$

Aiming at a coupling strength $r \simeq 1$ at a frequency around 5 GHz, one gets, $Z_C \sim 2k\Omega$, $L \sim 60$ nH and $C \sim 15$ fF.

In order to reduce the capacitance we fabricated the resonator on a quartz wafer, with a small effective permittivity $\epsilon_r = 4.2$ (in comparison with 11.8 for silicon).

Planar coils [52, 53] offer an increased inductance compared to transmission lines resonators [54], and better linearity than Josephson based resonators [55]. They have, however, one main disadvantage : their center has to be connected either to the Josephson junction or to the detection line, using either bonding wires [53] or bridges [52]. Both solutions have a non negligible influence on the resonator. Bonding wires require bonding pad with typical size $50 \mu\text{m}$, which increases the capacitance to ground, where as a bridge forms a capacitor with every turn of the coil that must be taken into account in the microwave simulations.

We chose to use an Aluminum bridge, supported by a $> 1\mu\text{m}$ BCB layer. BCB is a low loss dielectric which has been developed for such applications by the microwave industries which also has a relatively low permittivity.

A last parameter of the resonator that can be tuned is its quality factor Q . We consider a simple parallel LC oscillator with

$$Q = \frac{f_0}{\Delta f} = \frac{Z_C}{Z_{\text{Det}}},$$

where Z_{Det} is the impedance of the detection line as seen from the resonator and Δf the resonance bandwidth at -3dB. To tune Q , we can insert an impedance transformer between the 50Ω measurement line and the resonator and thus increase the effective input impedance, to decrease the quality factor.

In order to simulate our resonators, we use a high frequency electromagnetic software tool for planar circuits analysis : Sonnet. The system simulated by this software consists in several metallic layers separated by dielectrics as shown in Fig. S5.

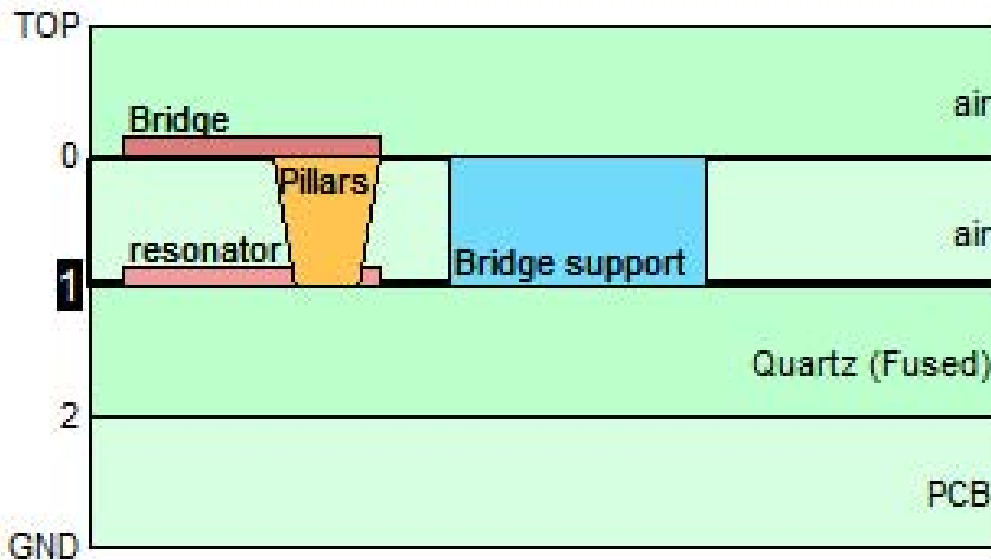


FIG. S5: Sonnet schematic of the dielectric stack.

Each metallic sheet layer contains a metallic pattern for the circuit, with strip-lines or resonators and can be connected to the other layers through vias. Dielectric layers properties and thickness can also be chosen.

This stack is enclosed in a box with perfect metallic walls. The simulated device sees the outer world through ports that sit at the surface of the box, or are added inside the box, as probes shown in Fig. S6. Sonnet also allows us to insert lumped electric component in the circuit, between two points of the pattern.

As we are interested in the behavior of the environment seen by the junction, we will replace it by a port, which will act like a probe. We assume that the Josephson energy is small enough for the admittance of the junction associated to the flow of Cooper pairs to be negligible ; we can thus model the junction as an open port. Furthermore, in order to take into account the junction's geometric capacitance, we add a discrete capacitor in parallel to ground as presented in Fig. S6. The other port of the resonator is model by a 50Ω resistor, modeling the detection line.

Using the microwave simulation results, we predict the resonant frequency f_0 , the impedance seen by the junction $Z_{\text{out}2}$, the quality factor Q and the environment characteristic impedance Z_C .

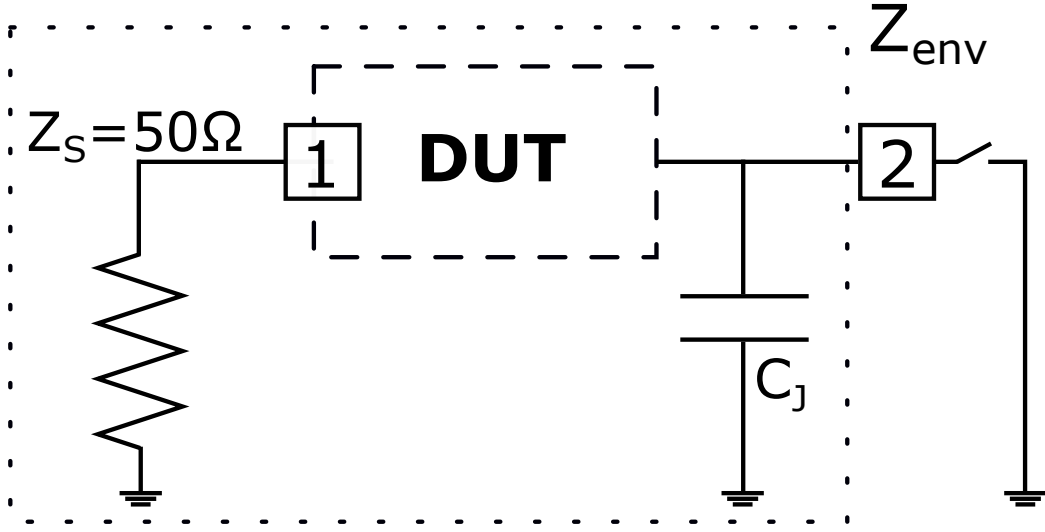


FIG. S6: Sonnet port configuration.

Coil	nb of turns	line width	line space	bridge
	23.5	1 μ m	2 μ m	BCB / 1.2 μ m
Results	f_0	Δf	Z_C	$\text{Re}(Z_{\text{env}})_{\text{MAX}}$
($C_J = 2$ fF)	5,1 GHz	60 MHz	2,05 k Ω	188k Ω

TABLE I: Geometric parameters of the resonator and associated characteristics.

The corresponding schematic and result of simulations are shown in Fig. S7. Now, the lumped capacitor C_J represents the capacitance of the Josephson junction alone, the rest of the capacitance being implemented by the surrounding ground.

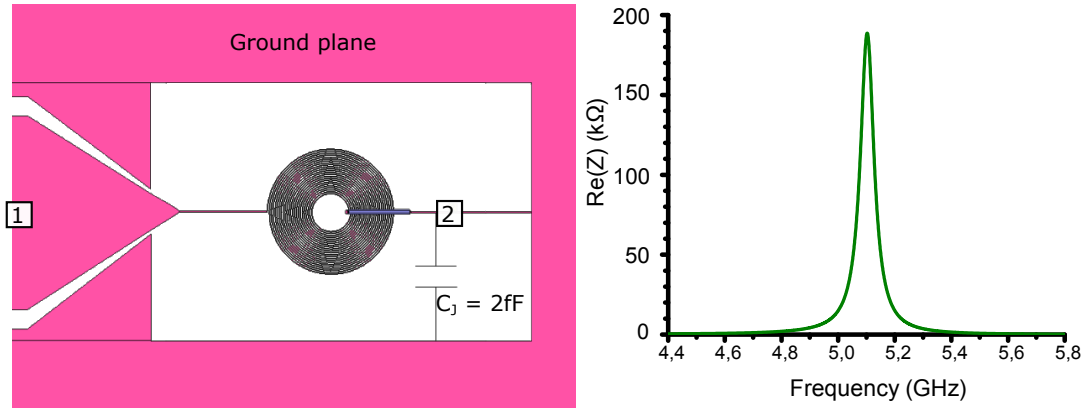


FIG. S7: Final design drawing (left) and associated simulation result(right).

Computing current densities In order to understand the full resonator behavior, we have simulated current and charge densities at resonance, as shown in Fig. S8.

Resonator : impedance transformer

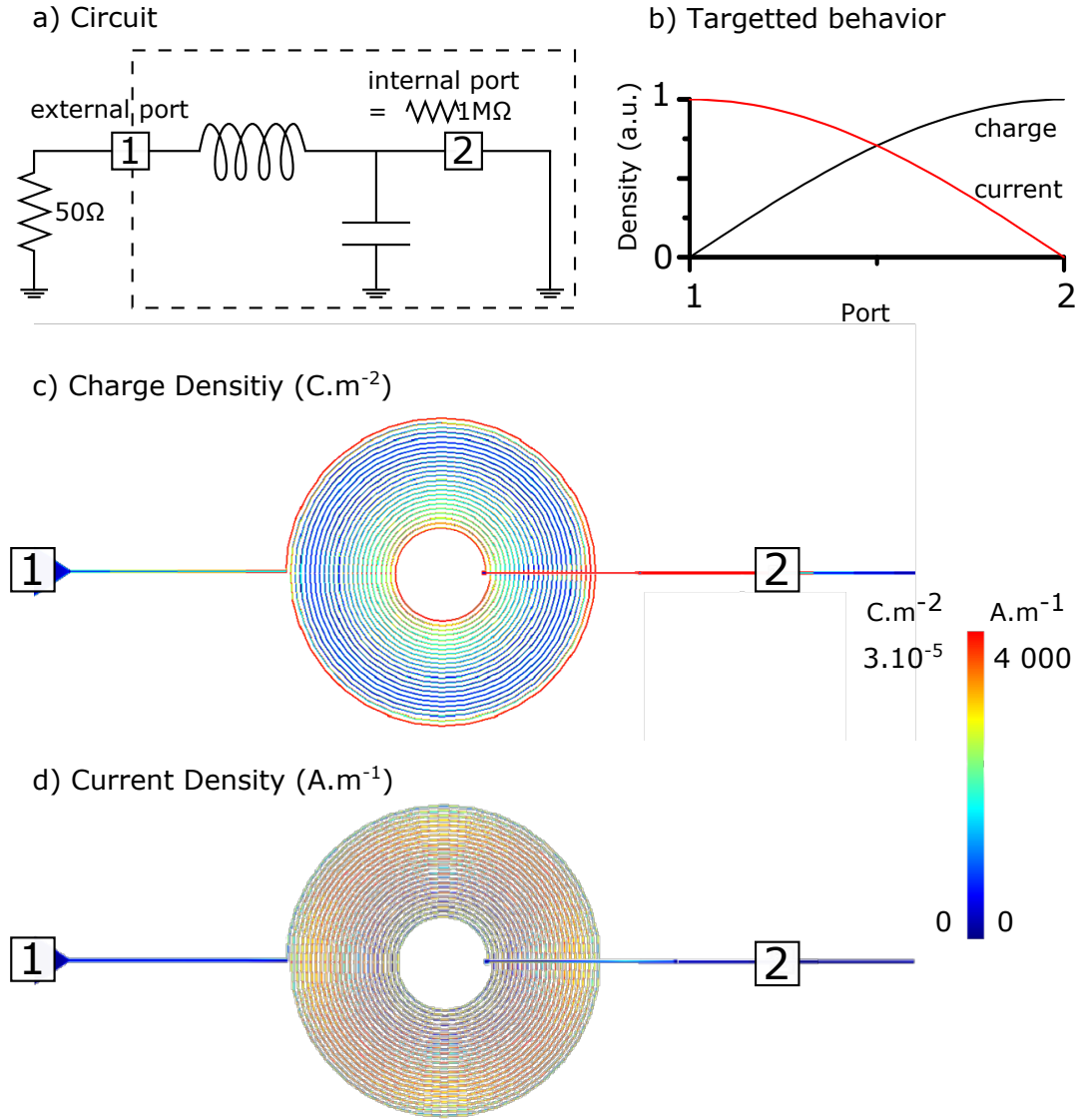


FIG. S8: a) Our circuit has two ports. One external port “1” to be connected to the measurement chain can be modeled as a 50Ω load. The second port “2” is internal to the circuit and parametrized to mimic the Josephson junction open between the resonator and the ground plane probes the impedance seen by the future junction. These boundary conditions make us expect the resonator to behave like a $\lambda/4$ resonator. b) In a typical $\lambda/4$, the low impedance port 1 corresponds to a node in charge and an anti-node in current, while on the “open” side port 2, there is an accumulation of charges and no current. c) As expected, there is a charge accumulation on the high impedance side of the resonator. As the coil is used as an inductance but is also the capacitance of the circuit, there is an accumulation of charge at the periphery, i.e. in the first turn of the coil. d) There is indeed no current flowing through the high impedance side and we see an increase toward the low impedance port. in c) and d) the ground plane shown in fig. S7 is not represented here as it does not present peculiar current/charge density.

Junction’s capacitance influence

The Josephson junction’s geometric capacitance C_J is of the order of few fF ($70 \text{ fF} \cdot \mu\text{m}^{-2}$) [56] and is also part of the environment seen by the pure Josephson element according to

$$Z_{\text{env}}(\omega) = \frac{Z_{\text{circuit}}(\omega)}{1 + jC_J\omega Z_{\text{circuit}}(\omega)},$$

where $Z_{\text{circuit}}(\omega)$ is the impedance of the resonant circuit connected to the measurement line without junction.

By adding a discrete capacitor to ground $C = C_J$ (cf. Fig. S7) at the junction's position in simulations and tuning its value, one can then observe in Fig. S9 that it is not negligible and must be taken into account.

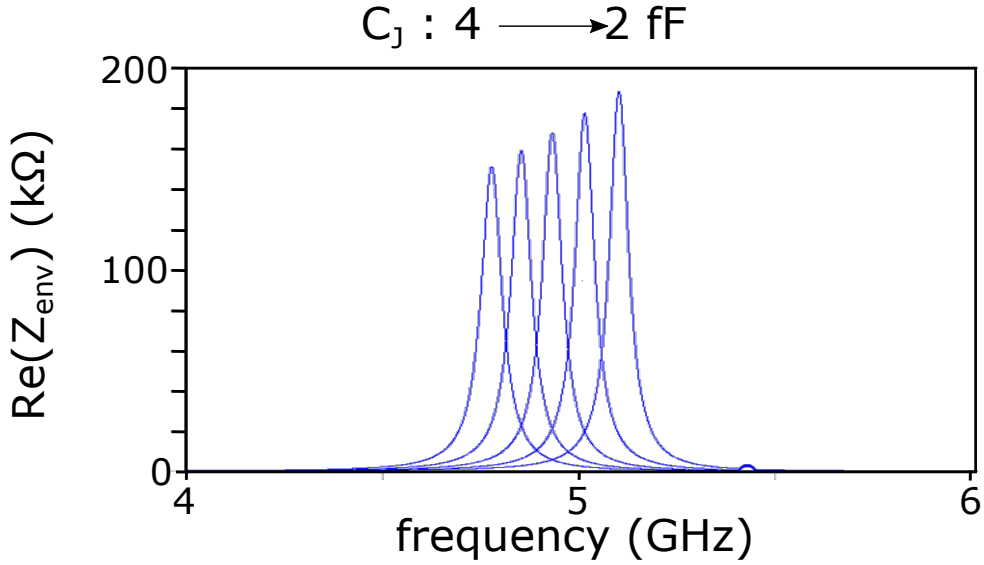


FIG. S9: Real part of the impedance seen by the junction $\text{Re}[Z_{\text{env}}(\omega)]$ for different junction capacitances

As we aim at building a resonator with a capacitance around 15 fF, C_J will account for 10 to 20% of the total capacitance of the circuit. As a consequence, both characteristic impedance and resonant frequency will be decreased by 5 to 10%.

Tuning the bandwidth using quarter wavelength resonator

According to table I and Fig. S7, our resonator is expected to have a bandwidth of $\Delta f \sim 60$ MHz, which is not much larger than the 3 MHz FWHM of the Josephson radiation due to low frequency voltage polarisation noise. It is thus useful to broaden this resonance while preserving the characteristic impedance and resonant frequency.

Keeping the same resonator geometry, one can enlarge its bandwidth by inserting a second resonator between it and the source to play the role of an impedance transformer (quarter wavelength). Doing so, we can increase the input impedance seen by the coil and broaden the resonance.

We have built this second stage of impedance transformer “on chip” between the measurement line (modeled by Z_0) and the coil, using a lossless coplanar waveguide (CPW) of length $l = \lambda/4$ according to :

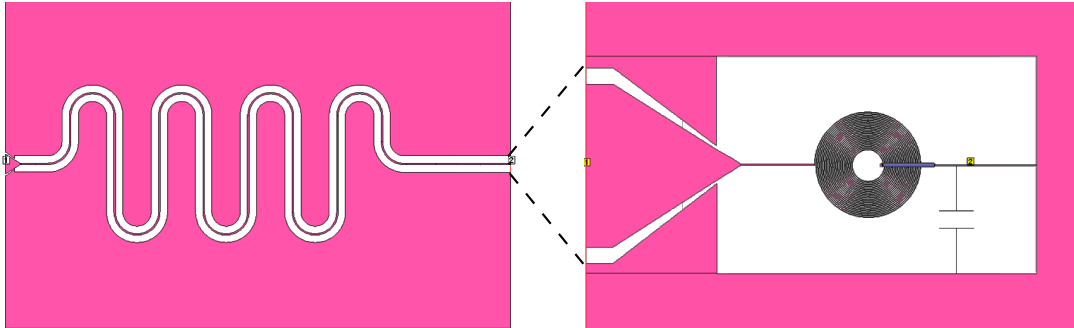


FIG. S10: Circuit with an additional impedance transformer.

Δf (MHz)	Z_{Det}	$Z_C, \lambda/4$	width(μm)	Gap (μm)
60	50	-	-	-
100	100	70	25	10
300	400	140	10	50
500	600	173	5	67

TABLE II: Influence of an additionnal impedance transformer on the resonator bandwidth.

This transformer is characterized by

$$Z_{\text{Det}} = \frac{Z_C^2}{Z_0},$$

where Z_C is the characteristic impedance of the line, Z_{Det} the transformed detection impedance of the resonator and Z_0 the 50Ω characteristic impedance of the detection line.

One can then choose the impedance seen by the coil (the impedance Z'_0 of the transformer) by tuning the characteristic impedance Z_C . To do so, textbook calculations allow to choose the good ratio between the width of the central conductor and the distance to ground plane on a particular substrate [57]. The bandwidth of the resonator, corresponding to an input impedance of 50Ω , is 60 MHz. By adding quarter wavelength transformers, we increase Δf as listed in table :

Using the quarter wavelength transformer simulations as a first block and the previous coil results as a second one, the full circuit was simulated, using the Sonnet “netlist” feature. Such a combination of previous simulations assumes no geometric “crosstalk” between the two resonators, which makes sense given that they are shielded from each other by ground planes. We obtained the results of Fig. S11.

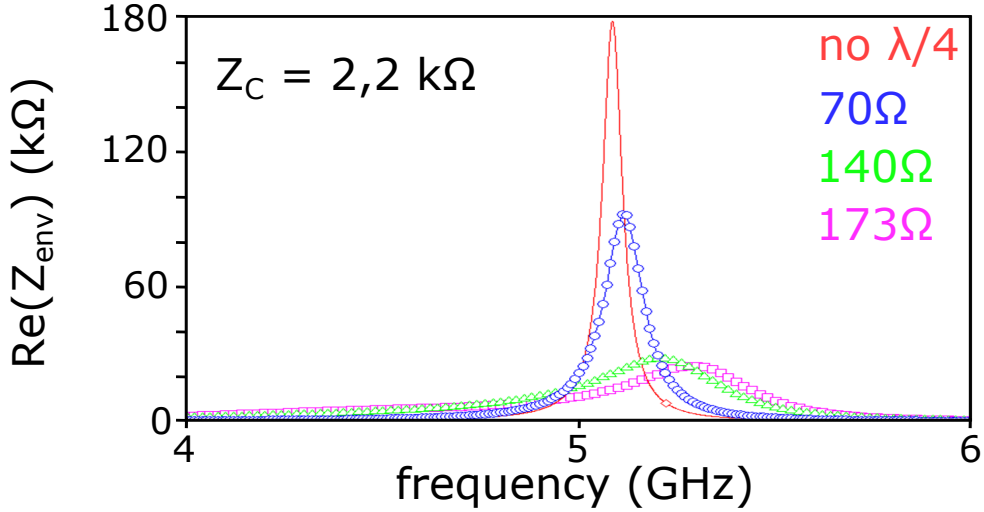


FIG. S11: : initial simulation result and Netlist simulation results for the 3 $\lambda/4$ transformers of table

We were then able to check that the $\lambda/4$ resonator has no influence on the characteristic impedance by extracting it for each design. In order to have different bandwidth, these four configurations were fabricated. In practice, the sample used in the experiments reported in the main text had a 70Ω quarter wavelength inserted between the 50Ω detection line and the planar inductor resonator.

FABRICATION

As mentioned above, we built the circuit of Fig. S12 on a $3 \times 10 \text{ mm}^2$ low permittivity quartz chip with a single input/output port adapted to a 50Ω measurement line.

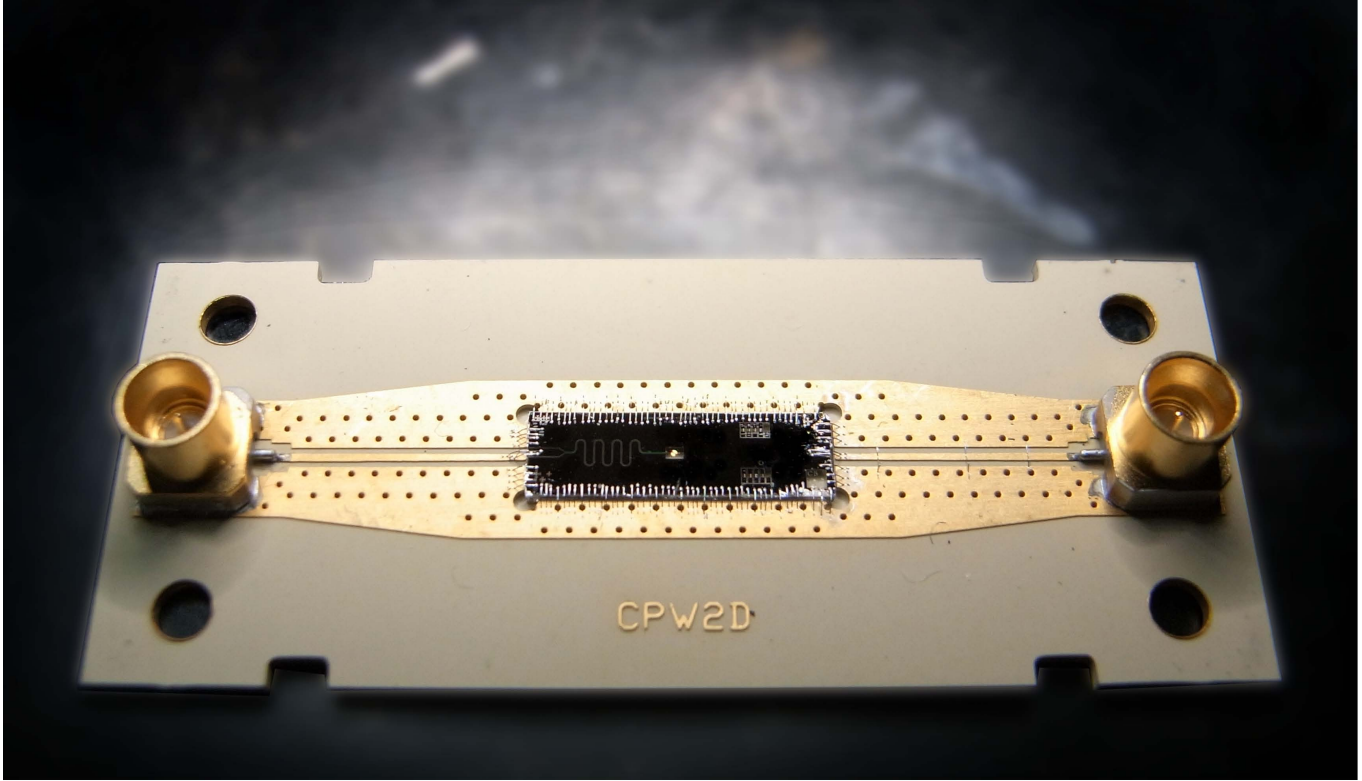


FIG. S12: Photograph of the chip used for the experiments described in the main text.

Our fabrication process consists in 3 main steps. First, we fabricate Niobium based coil and quarterwave impedance transformers. Then, we connect the center of the coil to its periphery with a bridge and finally, as it is the most fragile element, we fabricate the Josephson junctions.

Resonator: coil and $\lambda/4$

In order to be able to test the samples at 4K, we chose to build niobium based resonator. As Niobium is of a much better quality when sputtered than evaporated, we used a top down approach for this step.

A 100 nm layer of Niobium was first deposited on a $430\mu\text{m}$ thick Quartz wafer at 2nm/s using a dc-magnetron sputtering machine and then patterned by optical lithography and reactive ion etching (RIE).

In order to pattern the resonators, we used an optical lithography process. The classical optical lithography process used a resist thick enough so that all the niobium between the lines can be removed before all the resist is etched, the S1813 from Shipley.

It was spun according to the following recipe:

1. 110C prebake of the substrate on hot plate
2. Resist spinning : S1813, 4000 rpm 45" / 8000 rpm 15"
3. 2 min rebake on hot plate

Using these parameters, and performing interferometric measurements, we measured a resist layer of 1450 nm. The sample was then exposed with a Karl-Süss MJB4 optical aligner, with a dose of 150 mJ/cm^{-2} (15 secs). Finally it was developed using microposit MF319 during 90 seconds and rinsed in deionized water for at least 1 min.

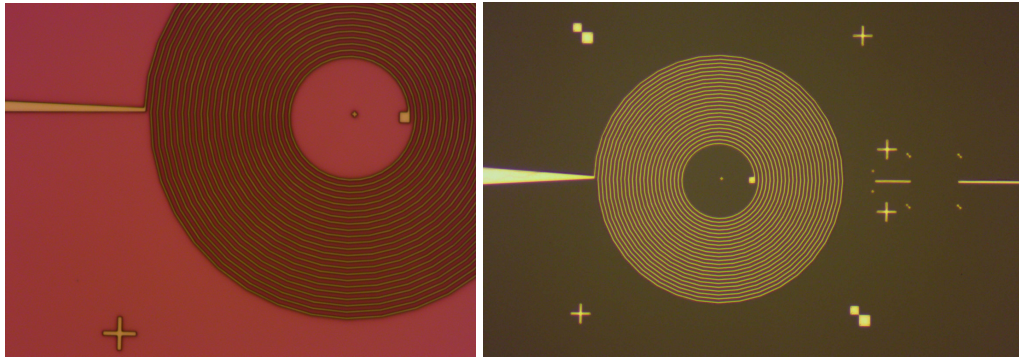


FIG. S13: Fabrication of the coil. Left : photograph after optical lithography. Right : photograph after niobium etching.

The next step of the process is the reactive ion etching of the niobium film : we used a mixture of CF_4 and Ar (20/10 cc) at a pressure of $50\mu\text{bar}$ (plasma off) and a power of 50 W (209V) for 4 minutes 45 seconds (150 nm). After this process, the sample was cleaned in 40C acetone for 10 minutes to remove any resist residues and rinsed in IPA.

The quarter wave resonator was fabricated at the same time as the coil by Niobium etching.



FIG. S14: $70\ \Omega$ quarter wavelength impedance transformer and coil. The whole chip is $3 \times 10\ \text{mm}^2$.

Bridge

As we decided to use a dielectric spacer to support the bridge, we added two additional steps to the fabrication process. One for the dielectric spacer, the second one for the bridge itself. One of the main difficulties of these steps is that, as the pads to connect the bridge is small, they require very precise alignment.

Dielectric support We chose to work with polymers derived from B-staged bisbenzocyclobutene, sold as Cyclotene 4000 by Dow Chemicals and choose the lower viscosity, in order to obtain a spacer between 0.8 and $1.8\mu\text{m}$ thick: XU35133. The process was performed according to the following recipe:

1. 2 minutes prebake at 110 C
2. Primer AP 3000 rpm 30 secs
3. BCB XU : 3000rpm, 45secs/ 8000 rpm 15 secs
4. 3 minutes rebake @80 C

Using this technique, we obtained 1650 nm thick layers. The sample was then exposed with the MJB4 optical aligner, with during 3 seconds. The development of this resist is quite difficult as it is not dissolved by acetone:

1. 30 secs on hot plate (70 C) : to avoid that the bridge flows

2. DS 3000 rinsing for 1 minute
3. TS 1100 rinsing for 30 seconds
4. 1 min rinsing in deionized water
5. the sample was then dried while spinning

In order to obtain a flat surface and remove all resist residues, an RIE SF_6/O_2 etching was performed for 30 seconds (20/2 cc, $10\mu\text{bar}$, 50W) as shown in Fig S15. Finally, the sample was rebaked during 30 minutes at 190C to stabilize the resist.

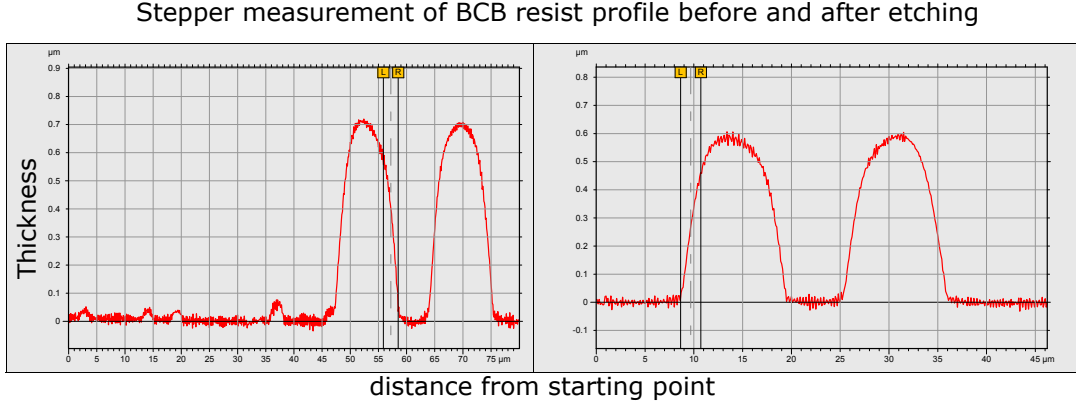


FIG. S15: The flatness of the sample was measured with a stepper. After 30 seconds of SF_6/O_2 etching, resist residues have disappeared

Bridge's line As the spacer is quite thick, this step requires a thicker resist. We used AZ5214 and obtained a $1.5\mu\text{m}$ layer of resist according to the recipe:

1. 72C prebake on hot plate
2. microposit primer : 6000rpm for 30 seconds
3. AZ5214 : 4000 rpm during 60s, 8000rpm during 10s
4. 2min rebake at 100C with a bescher on top of the sample

The sample was then aligned and exposed during 7s using the MJB4. As the AZ5214 is a negative resist which can be reversed, we rebaked the sample for 3min at 120C and performed a flood exposure for 25 seconds. The development was then performed using diluted AZ 400K with deionized water (1:4) for 1 min. Finally, the BCB was covered with a 200 nm layer of aluminum after 12 seconds Argon etching to ensure good contacts with the coil.

Josephson junction

As explained in the main text, for $r \simeq 1$, strong anti-bunching effects are expected when the resonator is, in average, almost empty. The maximum photon emission rate is given by

$$\dot{n} = \frac{\text{Re}[Z(\omega_0)]I_0^2}{2\hbar\omega_0},$$

from which the mean occupation number n can be deduced by:

$$\dot{n} = \frac{n}{\Gamma},$$

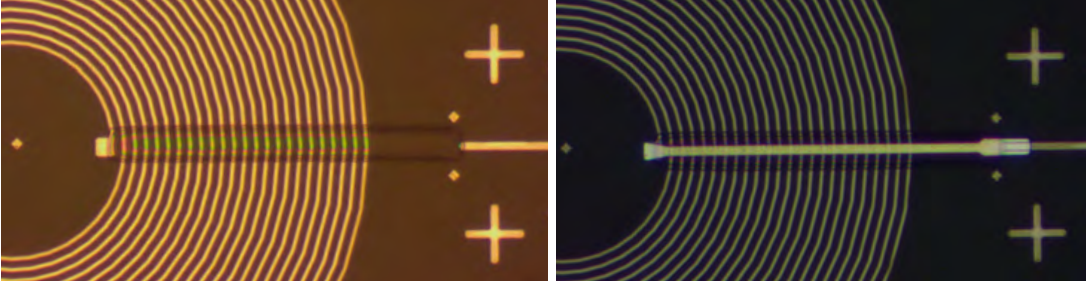


FIG. S16: Left: in a first step, a BCB brick is deposited with optical lithography. Right: in a second step the core of the coil is connected with an aluminum bridge.

with $\Gamma = 2\pi \text{HMBW}$, the leaking rate of the resonator. In order to estimate the targeted resistance of the junction, one uses the Ambegaokar-Baratoff formula and Josephson relations (taking into account that DCB will renormalizes E_J by a factor of $\exp(-\pi Z_C/2R_Q)$):

$$I_0 = \frac{\pi\Delta}{2eR_N}, \quad E_J = \frac{\varphi_0 I_C}{2\pi}.$$

In order to be able to tune E_J with a magnetic field, a SQUID geometry is used for the Josephson junction: two junctions are placed in parallel to form a loop, which behaves as a single effective junction tunable with the external magnetic flux applied to the loop.

As a small capacitance is required for the resonator, junctions must be as small as possible, but big enough to be reproducible and lead to a good symmetry between the two branches of the SQUID. Assuming a symmetry of 90%, E_J can then be reduced by a factor of 10 tuning the flux with a little coil on top of the sample.

Assuming a bandwidth $\Delta\omega \sim 100 \text{ MHz}$, a characteristic impedance $Z_C \sim 2k\Omega$, a critical current I_0 of 1 nA and a symmetry of 90%, one can estimate the minimal amount of photon in resonator :

$$n = 1/100 \cdot \frac{\dot{n}}{\Gamma} = \frac{Z_C I_0^2}{2h(\Delta\omega)^2 \cdot 100} e^{-\pi Z_C/R_Q} \sim 0.5$$

with $\Delta\omega$ the half maximum bandwidth of the resonator (FWHM). These parameters require a normal state resistance for the SQUID of $R_N \sim 300k\Omega$.

Fabrication principle Samples are made of aluminum based tunnel junctions, fabricated by double angle evaporation through a suspended shadow mask, using the standard Dolan technique [58]. By adjusting the angles of evaporation, two adjacent openings in the mask can be projected onto the same spot, creating an overlay of metallic films as shown in fig. S17. The first film is oxidized before the second evaporation to form the tunnel barrier.

In order to have reproducible as well as small junctions, we used a cross shape as shown in Fig. S18.

SQUID fabrication PMMA/PMGI resist bilayer spinning :

1. 2 min rebake at 110 C
2. Ti prime 6000 rpm 30 secs
3. PMGI SF8 : 3000rpm, 45secs/ 6000 rpm 15 secs ($\approx 613 \pm 15\text{nm}$)
4. 5min rebake @170C with bescher
5. PMMA A6 : 6000rpm, 60secs ($\approx 253 \pm 21\text{nm}$)
6. 15 min rebake @ 170C (with bescher)

As the quartz is very sensitive to charging effects, we placed an additional 7nm layer of aluminum on top of the resist to evacuate charges during EBL. The full wafer was then covered by a thick layer of UVIII resist which can be removed in IPA and sent to IEF for dicing. Actually, as the Quartz substrate has a hexagonal symmetry, it cannot be cleaved.

We then performed EBL on single chips using an FEI XL30 SEM with a dose of $300 \mu\text{C} \cdot \text{cm}^{-2}$ at 30 kV. The focus was tuned a three point on the sample using 20 nm gold colloids.

The development process then consisted in :

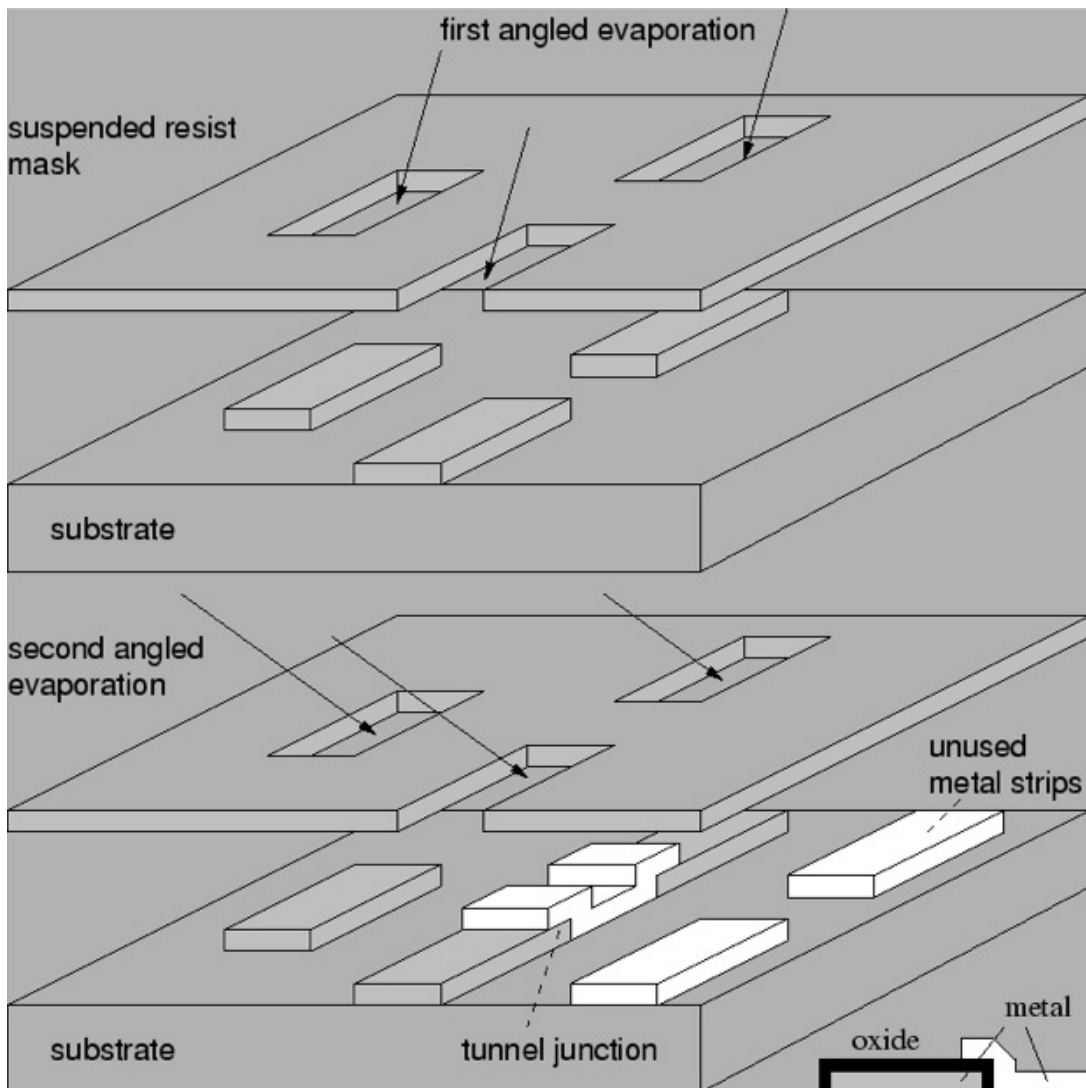


FIG. S17: Double angle evaporation principle: two metallic layers are evaporated onto the same spot, creating an overlay of metallic films. As the first layer was oxidized, the two electrodes are separated by an insulator and form a Josephson SIS junction.

1. 35 secs MIF 726, 15 secs ODI to remove the aluminum layer
2. 60 secs MIBK + IPA (1:3), 30 secs IPA, 15 secs ODI to open the Josephson junction patterns
3. 25 secs MIF 726, 1min ODI, 15 secs ethanol to have a nice undercut

Double oxidation junctions Finally, we deposited and oxidized aluminum to form highly resistive Josephson junctions using double angle evaporation technique. In order to fabricate very resistive Josephson junctions, the group of J.P. Pekola [56] raised the idea of oxidizing not one layer of aluminum but to do it twice. By evaporating an additional subnanometer thick layer of Al immediately after oxidizing the first layer, and oxidizing this fresh very thin layer, one thus obtain thicker barriers.

The key parameter of this recipe is the thickness of the intermediate thin Al layer. As it will be completely oxidized we can achieve resistances up to $1M\Omega$ with 0,4nm. Using this process, the surfacic capacitance of the junction is estimated to $70\text{ fF}/\mu\text{m}^2$ i.e. $\sim 2\text{ fF}$ for the SQUID.

1. Argon ion milling 2×10 secs / 3 mA

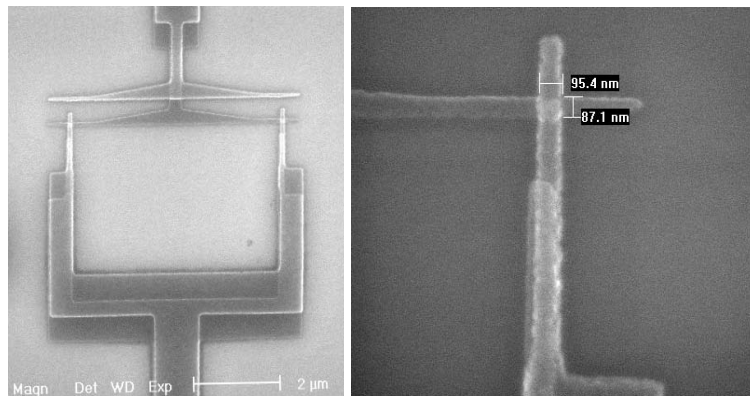


FIG. S18: Left: SEM image of the SQUID. Right: zoom on one of the Josephson junction with size $95 \times 87 \text{ nm}^2$

2. -24 : 20 nm Al @ 1 nm.s-1
3. O₂/Ar (15/85 %) oxidation 300 mbar during 20 min
4. 0.25 nm Al @ 0.1 nm.s-1
5. O₂/Ar (15/85 %) oxidation 667 mbar during 10 min
6. 24 : 80 nm Al @ 1 nm.s-1

The lift-off of the resist was done by putting the sample in 60C remover-PG during 40 minutes. In order to get uniform resistance values and limit Josephson junctions aging, they were rebaked on a hot plate at 110C during one minute.

The chip was then stuck on the PCB with UV88 resist and bonded to the single input/ output port using aluminum wires as shown in Fig. S12.

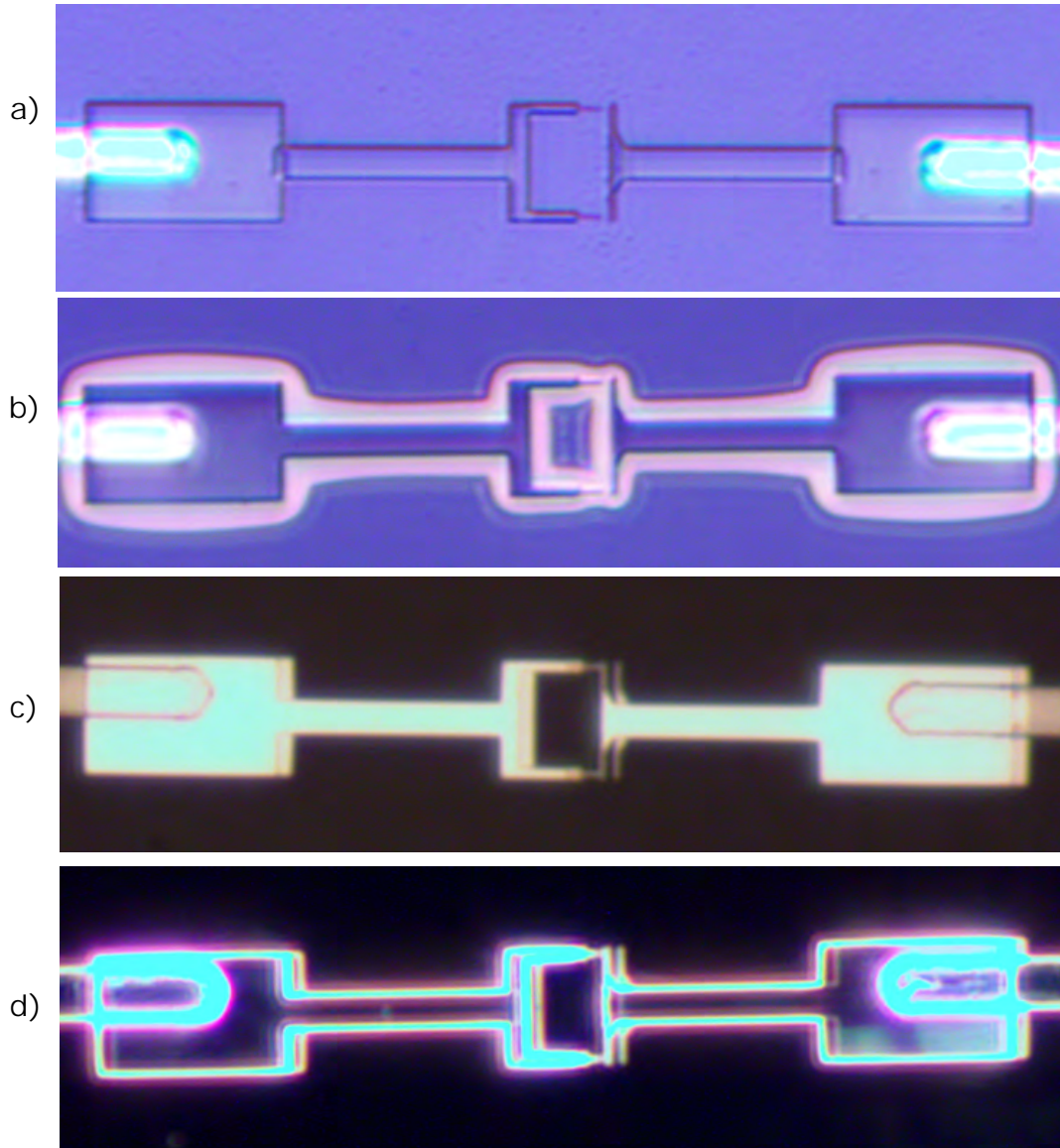


FIG. S19: Josephson junction fabrication steps : a) Josephson junction shape : PMMA development b) Undercut : PMGI development c) & d) optical microscope view of the junctions after lift-off

Inductive-detection electron-spin resonance spectroscopy with 65 spins/ Hz sensitivity

S. Probst, A. Bienfait, P. Campagne-Ibarcq, J. J. Pla, B. Albanese, J. F. da
Silva Barbosa, T. Schenkel, D. Vion, D. Esteve, K. Mølmer, et al.

► **To cite this version:**

S. Probst, A. Bienfait, P. Campagne-Ibarcq, J. J. Pla, B. Albanese, et al.. Inductive-detection electron-spin resonance spectroscopy with 65 spins/ Hz sensitivity. Applied Physics Letters, American Institute of Physics, 2017, 111 (20), pp.202604. 10.1063/1.5002540 . hal-01664352

HAL Id: hal-01664352

<https://hal.archives-ouvertes.fr/hal-01664352>

Submitted on 14 Dec 2017

HAL is a multi-disciplinary open access archive for the deposit and dissemination of scientific research documents, whether they are published or not. The documents may come from teaching and research institutions in France or abroad, or from public or private research centers.

L'archive ouverte pluridisciplinaire **HAL**, est destinée au dépôt et à la diffusion de documents scientifiques de niveau recherche, publiés ou non, émanant des établissements d'enseignement et de recherche français ou étrangers, des laboratoires publics ou privés.

Inductive-detection electron-spin resonance spectroscopy with 65 spins/ $\sqrt{\text{Hz}}$ sensitivity

S. Probst,^{1, a)} A. Bienfait,^{1, 2} P. Campagne-Ibarcq,^{1, 3} J. J. Pla,⁴ B. Albanese,¹ J. F. Da Silva Barbosa,¹ T. Schenkel,⁵ D. Vion,¹ D. Esteve,¹ K. Mølmer,⁶ J. J. L. Morton,⁷ R. Heeres,¹ and P. Bertet¹

¹⁾ *Quantronics group, SPEC, CEA, CNRS, Université Paris-Saclay, CEA Saclay 91191 Gif-sur-Yvette Cedex, France*

²⁾ *Institute for Molecular Engineering, University of Chicago, Chicago, Illinois 60637, USA*

³⁾ *Departments of Applied Physics and Physics, Yale University, New Haven, CT 06520, USA*

⁴⁾ *School of Electrical Engineering and Telecommunications, University of New South Wales, Anzac Parade, Sydney, NSW 2052, Australia*

⁵⁾ *Accelerator Technology and Applied Physics Division, Lawrence Berkeley National Laboratory, Berkeley, California 94720, USA*

⁶⁾ *Department of Physics and Astronomy, Aarhus University, Ny Munkegade 120, DK-8000 Aarhus C, Denmark*

⁷⁾ *London Centre for Nanotechnology, University College London, London WC1H 0AH, United Kingdom*

(Dated: 31 August 2017)

We report electron spin resonance spectroscopy measurements performed at millikelvin temperatures in a custom-built spectrometer comprising a superconducting micro-resonator at 7 GHz and a Josephson parametric amplifier. Owing to the small $\sim 10^{-12} \lambda^3$ magnetic resonator mode volume and to the low noise of the parametric amplifier, the spectrometer sensitivity reaches 260 ± 40 spins/echo and 65 ± 10 spins/ $\sqrt{\text{Hz}}$, respectively.

PACS numbers: 07.57.Pt, 76.30.-v, 85.25.-j

Electron spin resonance (ESR) is a well-established spectroscopic method to analyze paramagnetic species, utilized in materials science, chemistry and molecular biology to characterize reaction products and complex molecules¹. In a conventional ESR spectrometer based on the so-called inductive detection method, the paramagnetic spins precess in an external magnetic field B_0 and radiate weak microwave signals into a resonant cavity, whose emissions are amplified and measured.

Despite its widespread use, ESR has limited sensitivity, and large amounts of spins are necessary to accumulate sufficient signal. Most conventional ESR spectrometers operate at room temperature and employ three-dimensional cavities. At X-band², they require on the order of $\sim 10^{13}$ spins to obtain sufficient signal in a single echo¹. Enhancing this sensitivity to smaller spin ensembles and eventually the single-spin limit is highly desirable and is a major research subject. This has been achieved by employing alternative detection schemes including optically detected magnetic resonance (ODMR)^{3,4}, scanning probe based techniques⁵⁻⁹, SQUIDS¹⁰ and electrically detected magnetic resonance^{11,12}. For instance, ODMR achieves single spin sensitivity through optical readout of the spin state. However, this requires the presence of suitable op-

tical transitions in the energy spectrum of the system of interest, which makes it less versatile.

In recent years, there has been a parallel effort to enhance the sensitivity of inductive ESR detection¹³⁻²⁰. This development has been triggered by the progress made in the field of circuit quantum electrodynamics (cQED)²¹, where high fidelity detection of weak microwave signals is essential for the measurement and manipulation of superconducting quantum circuits. In particular, it has been theoretically predicted²² that single-spin sensitivity should be reachable by combining high quality factor superconducting micro-resonators and Josephson Parametric Amplifiers (JPAs)²³, which are sensitive microwave amplifiers adding as little noise as allowed by quantum mechanics to the incoming spin signal. Based on this principle, ESR spectroscopy measurements¹⁸ demonstrated a sensitivity of 1700 spins/ $\sqrt{\text{Hz}}$. In this work, we build on these efforts and show that, by optimizing the superconducting resonator design, the sensitivity can be enhanced to the level of 65 spins/ $\sqrt{\text{Hz}}$.

Figure 1(a) shows a schematic design of the spectrometer consisting of a superconducting LC resonant circuit capacitively coupled to the measurement line with rate κ_c and internal losses κ_i . The resonator is slightly over-coupled ($\kappa_c \gtrsim \kappa_i$) and probed in reflection at its resonance frequency ω_r . This micro-resonator is inductively coupled to the spin ensemble and cooled to 12 mK in a dilution refrigerator. The signal leaking out of the resonator, which contains in particular the spin signal,

^{a)} sebastian.probst@cea.fr

is first amplified by a JPA operating in the degenerate mode^{24,25}, followed by a High-Electron-Mobility Transistor (HEMT) amplifier at 4 K and further amplifiers at room-temperature. The two signal quadratures $I(t)$ and $Q(t)$ are obtained by homodyne demodulation at ω_r . More details on the setup can be found in Ref. 18.

Compared to Ref. 18, the micro-resonator was re-designed with the goal of enhancing the spin-resonator coupling constant $g = \gamma_e \langle 0 | S_x | 1 \rangle \delta B_1$, where $\langle 0 | S_x | 1 \rangle \approx 0.5$ for the transition used in the following. Here, $\gamma_e/2\pi = 28$ GHz/T denotes the gyromagnetic ratio of the electron, $|0\rangle$ and $|1\rangle$ the ground and excited state of the spin, \mathbf{S} the electron spin operator and δB_1 the magnetic field vacuum fluctuations. Reducing the inductor size to a narrow wire decreases the magnetic mode volume²⁶ and therefore enhances δB_1 . In the new design, shown in Fig. 1b, most of the resonator consists of an interdigitated capacitor, shunted by a $l = 100 \mu\text{m}$ long, $w = 500$ nm wide, and $t = 100$ nm-thick wire inductance. It is patterned out of an aluminum thin-film by electron-beam lithography followed by lift-off, on top of an isotopically enriched ^{28}Si sample containing bismuth donors implanted at a depth of $z \approx 100$ nm. Based on electromagnetic simulations, an impedance of 32Ω and a magnetic mode volume of $\sim 10^{-12} \lambda^3$ (0.2 pico-liters) are estimated, resulting in a spin-resonator coupling of $g/2\pi \approx 4.3 \cdot 10^2$ Hz. The resonator properties are characterized at 12 mK by microwave reflection measurements^{27,28}, yielding $\omega_r/2\pi = 7.274$ GHz, $\kappa_c = 3.4 \cdot 10^5 \text{ rad s}^{-1}$, $\kappa_i = 2.5 \cdot 10^5 \text{ rad s}^{-1}$ and a total loss rate of $\kappa_l = \kappa_i + \kappa_c = 5.9 \pm 0.1 \cdot 10^5 \text{ rad s}^{-1}$, measured at a power corresponding to a single photon on average in the resonator²⁹.

At low temperatures, bismuth donors in the silicon sample trap an additional valence electron to the surrounding host silicon atoms, which can be probed through electron spin resonance.^{30,31} The electron spin $S = 1/2$ experiences a strong hyperfine interaction ($A/2\pi = 1.45$ GHz) with the ^{209}Bi nuclear spin $I = 9/2$ giving rise to a zero field splitting of 7.38 GHz. The full Hamiltonian is given by $H/\hbar = \gamma_e \mathbf{S} \cdot \mathbf{B} - \gamma_n \mathbf{I} \cdot \mathbf{B} + A \mathbf{S} \cdot \mathbf{I}$, where $\gamma_n/2\pi = 7$ MHz/T denotes the gyromagnetic ratio of the nucleus. Note that the Bi spin system is also interesting in the context of quantum information processing because it features clock transitions where the coherence time can reach 2.7 s³². In addition, the large zero field splitting makes this system well suited for integration with superconducting circuits. Figure 1(c) shows the low field spectrum of the ESR-allowed transitions close to the resonator frequency. The dashed line marks the spectrometer resonator frequency at $\omega_r/2\pi = 7.274$ GHz.

For the sensitivity of the spectrometer, two quantities are relevant: the minimum number of spins N_{min} necessary to produce a single echo with a signal-to-noise ratio (SNR) of 1, as well as the number of spins that can be measured with unit SNR within 1 second of in-

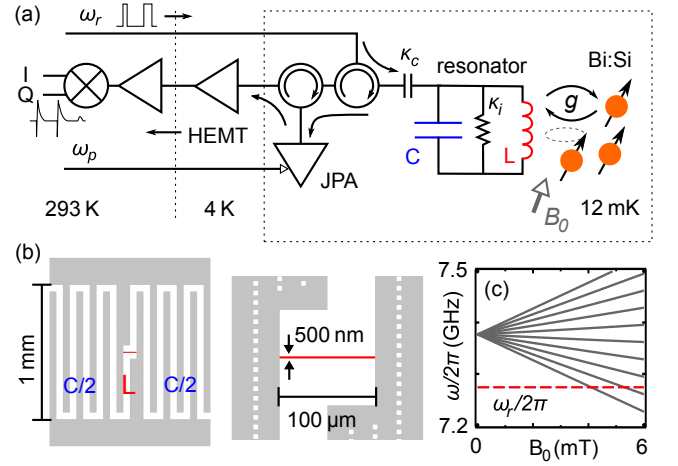


FIG. 1. (a) Schematic of the experiment: Bi:Si spins, biased by a dc magnetic field B_0 , are coupled to a LC resonator of frequency ω_r . Microwave control pulses at ω_r are sent onto the resonator input. The reflected signal, as well as the signals emitted by the spins, are first amplified by a JPA operated in degenerate mode followed by further amplification and homodyne demodulation to obtain the signal quadratures $I(t)$ and $Q(t)$. (b) Design of the planar lumped element LC resonator. (c) ESR-allowed transitions of the Bi donor spins vs. B_0 . Dashed line indicates the resonator frequency.

tegration time $N_{min}/\sqrt{N_{seq}}$ where N_{seq} is the number of experimental sequences per second. This timescale is determined by the spin energy relaxation time T_1 , and we typically wait $T_{rep} \gtrsim 3T_1$ between measurements. In our experiment, the lowest transition of the Bi ensemble is tuned into resonance with the cavity by applying $B_0 = 3.74$ mT parallel to the central inductor. In order to address all spins within the cavity bandwidth, we choose the duration t_p of our square pulses $0.5 \mu\text{s}$ for the $\pi/2$ and $1 \mu\text{s}$ for the π pulse such that $t_p \kappa_l \lesssim 1$. The π pulse amplitude was determined by recording Rabi oscillations on the echo signal, see Fig. 2(c). Figure 2(a) shows a full echo sequence (red circles). The reflected control pulses show a rapid rise followed by a slower decay due to the resonator ringdown, leading to an asymmetric echo shape.

In order to simulate the data, knowledge of g is necessary¹⁸. It is experimentally obtained from spin relaxation data, as explained in the next paragraph, leaving no other adjustable parameter than the number of spins excited by the first $\pi/2$ pulse. The quantitative agreement, see blue line in Fig. 2(a), allows us to state that $N_e = 234 \pm 35$ spins are contributing to the echo. N_e is defined through the polarization created by the first $\pi/2$ pulse. For details on the simulation we refer to Ref. 18. The ESR signal is given by the echo area A_e and in order to extract the SNR, a series of echo traces was recorded. Each echo trace is then integrated, weighted by its expected mode shape, which constitutes a matched filter maximizing the SNR¹⁸. From the resulting histogram, shown in Fig. 2(b), we deduce a SNR

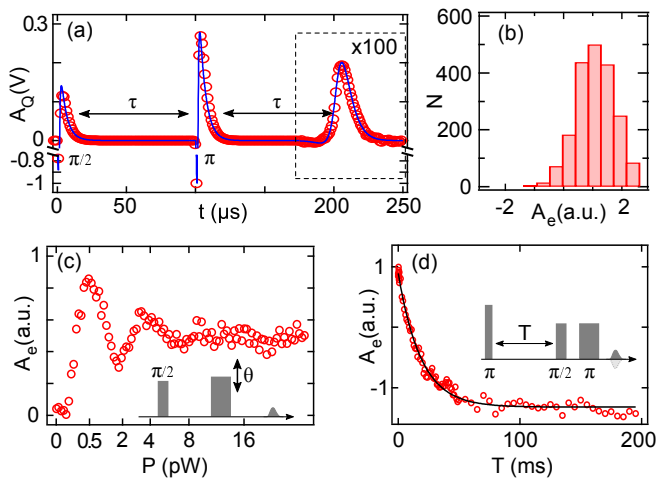


FIG. 2. (a) Measured (red circles) and simulated (blue line) quadrature signal showing the π and $\pi/2$ pulses as well as the echo. (b) Histogram of A_e . These data are obtained by subtracting two consecutive experimental traces with opposite $\pi/2$ pulse phases (phase cycling¹⁸), so that the single-echo SNR is obtained from the histogram width multiplied by $\sqrt{2}$. (c) Rabi oscillations of A_e , recorded by varying the power of the second pulse of the spin echo sequence. (d) Spin relaxation time measurement. A_e measured as a function of the delay T between an initial $1\ \mu\text{s}$ -long π pulse and a subsequent spin-echo sequence (red open circles). An exponential fit (black solid line) yields $T_1 = 18.6\ \text{ms}$.

of 0.9 per single trace, yielding a single shot sensitivity of $N_{\min} = 260 \pm 40$ spins per echo. This result is consistent with an estimate of $N_{\min}^{(\text{th})} = \frac{\kappa_l}{2gp} \sqrt{\frac{nw}{\kappa_c}} \approx 10^2$ spins using the theory developed in Ref. 18. Here, $n = 0.5$ is the number of noise photons, $p = 1 - \exp(-3T_1/T_1)$ the polarization and $w \approx \kappa_l$ the effective inhomogeneous spin linewidth. Since the experiment was repeated at a rate of 16 Hz, this single echo sequence translates into an absolute sensitivity of 65 ± 10 spins/ $\sqrt{\text{Hz}}$. This figure may be increased further by irradiating the resonator with squeezed vacuum, as demonstrated in Ref. 33.

Figure 2(d) shows the longitudinal decay of the spin ensemble. It was obtained with an inversion recovery pulse sequence: first, a $1\ \mu\text{s}$ -long π pulse inverts the spin ensemble followed by a spin echo detection sequence with $5\ \mu\text{s}$ and $10\ \mu\text{s}$ -long pulses after a variable time T . The exponential fit yields $T_1 = 18.6 \pm 0.5\ \text{ms}$. As shown in Ref. 34, the energy relaxation of donors in silicon coupled to small-mode-volume and high-quality-factor resonators is dominated by spontaneous emission of microwave photons into the environment, at a rate $T_1^{-1} = 4g^2/\kappa_l$. This allows us to experimentally determine that $g/2\pi = 450 \pm 11\ \text{Hz}$, which is close to the value estimated from design.

With the current sensitivity of $65\ \text{spins}/\sqrt{\text{Hz}}$, more than 1 hour of integration time would be needed to measure a single spin with unit SNR. Since the in-

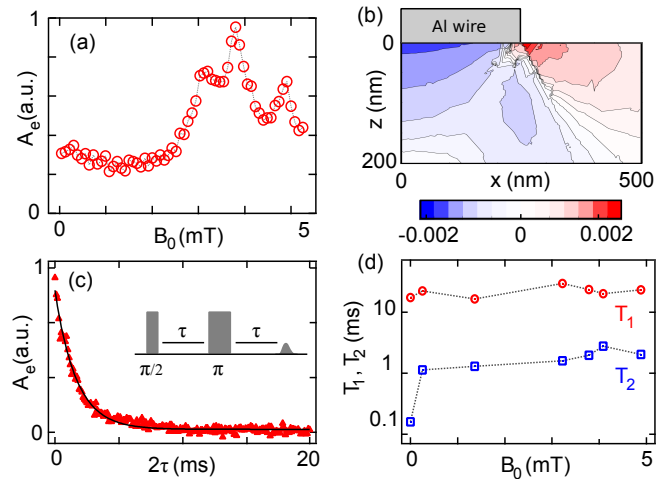


FIG. 3. (a) Echo-detected field sweep. A_e (open circles) is shown as a function of B_0 (parallel to the wire). (b) COMSOL[®] simulation of the ϵ_{100} component of the strain field in the silicon around the wire. (c) Spin coherence time measurement at $B_0 = 3.74\ \text{mT}$. A_e plotted as a function of the delay 2τ between $\pi/2$ pulse and echo (red triangles). An exponential fit (black solid line) yields $T_2 = 1.65 \pm 0.03\ \text{ms}$. (d) T_1 and T_2 as a function of B_0 . Error bars are within the marker size.

tegration time needed to accumulate a signal with a given SNR scales proportional to g^{-4} as explained in Ref. 22, increasing the coupling constant by one order of magnitude would be sufficient to obtain single-spin sensitivity in less than a second integration time. This can be achieved by bringing the spins closer to the inductor of the resonator using an even thinner and narrower inductor to concentrate δB_1 , and by reducing the impedance of the resonator further²⁰.

Figure 3(a) displays a Hahn-echo field sweep, i.e. A_e as a function of B_0 applied parallel to the inductor. The curve shows a large inhomogeneous broadening with Bi spins detected even at $B_0 = 0\ \text{mT}$, which are thus shifted by approximately 100 MHz from the nominal zero-field value, see Fig. 1(c). We attribute this broadening to strain exerted by the aluminum resonator onto the Si substrate resulting from a difference in their coefficients of thermal expansion^{18,35,36}. Figure 3(b) displays a COMSOL[®] simulation of the ϵ_{100} component of the strain tensor. The impact of strain on the Bi spectrum is subject of active experimental and theoretical research^{35,37}. We have investigated the dependence of the spin coherence and relaxation times on B_0 , as shown in Fig. 3(d). A typical coherence time measurement, recorded at $B_0 = 3.74\ \text{mT}$ by measuring A_e as a function of 2τ , is shown in Fig. 3(c). The data are well fitted by an exponential decay with $T_2 = 1.65 \pm 0.03\ \text{ms}$. While T_1 shows nearly no dependence on B_0 , T_2 decreases weakly towards lower magnetic fields and drops abruptly at zero field. This behavior might be due to fast dynamics

within the bismuth donor Zeeman sub-levels induced at low fields by a residual concentration of ^{29}Si nuclear spins, although more work is needed to draw a definite conclusion.

The sensitivity of the current spectrometer can be further enhanced by using multiple refocusing pulses to generate several echoes per sequence. Here, we employ the Carr-Purcell-Meiboom-Gill (CPMG) sequence^{1,38}, which consists of a $\pi/2$ pulse applied along the x-axis followed by n π pulses along the y-axis of the Bloch sphere. Assuming uncorrelated Gaussian noise, the increase of SNR is given by the CPMG echo decay curve $\text{SNR}(n)/\text{SNR}(1) = \frac{1}{\sqrt{n}} \sum_{i=1}^n A_e(t_i)$, where the index i labels the echoes from 1 to n along the sequence. The individual echoes during the first millisecond are presented in Fig. 4(a). The refocusing pulses are not visible in this plot because they are canceled by phase cycling. The blue line, computed by the simulation presented in Fig. 2(a) and using the same system parameters, is in good agreement with the data.

In order to quantify the gain in SNR, we record up to $4 \cdot 10^4$ single CPMG traces containing 200 echoes each. The data are then analyzed in two ways presented in Fig. 4(b) by dashed and solid lines, respectively: First, each echo in each sequence is integrated individually and its mean \bar{x}_i and standard deviation Δx_i are calculated in order to determine the $\text{SNR}_i = \bar{x}_i/\Delta x_i$ of the i -th echo. Provided that the noise is uncorrelated, the cumulative SNR sum over n echoes is given by $\text{SNR}_{\text{uncor}} = \frac{1}{\sqrt{n}} \sum_{i=1}^n \text{SNR}_i$. Second, we determine the actual cumulative $\text{SNR}_{\text{cum}} = \bar{x}_{\text{cum}}/\Delta x_{\text{cum}}$ by summing up all echoes in each trace up to the n -th echo and subsequently calculate the mean and standard deviation. Figure 4(b) shows the result for the spectrometer operating just with a HEMT amplifier, with the JPA in phase preserving mode and with the JPA in the degenerate mode. Without the JPA, $\text{SNR}_{\text{uncor}} \approx \text{SNR}_{\text{cum}}$ yielding a gain in SNR of up to 6. Employing the JPA, the gain initially follows the expectation for $\text{SNR}_{\text{uncor}}$ but then saturates. In particular, in the highest sensitivity mode, CPMG only allows for an increase in the SNR by approximately a factor of 2, thus reaching 33 spins/ $\sqrt{\text{Hz}}$. We interpret the discrepancy between SNR_{cum} and $\text{SNR}_{\text{uncor}}$ as a sign that correlations exist between the noise on the echoes of a given sequence, or in other words that low-frequency noise is present in our system.

To investigate whether this low-frequency noise is caused by the microwave setup (including the JPA), we perform a control experiment by replacing the echoes by weak coherent pulses of similar strength, which are reflected at the resonator input without undergoing any phase shift because they are purposely detuned by $\sim 25\kappa_l$ from ω_r . Figure 4(b) shows that $\text{SNR}_{\text{uncor}} = \text{SNR}_{\text{cum}}$ for this reference measurement (black dashed and solid lines are superimposed) indicating that the JPA itself is not responsible for the observed low frequency noise. Instead,

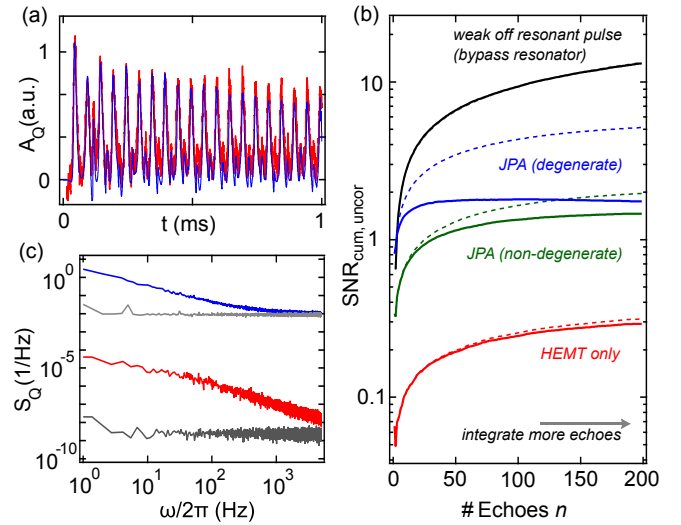


FIG. 4. (a) Averaged quadrature signal (red solid line) and simulation (blue solid line) showing the echoes recorded during the first millisecond of the CPMG sequence. (b) SNR vs. number of averaged CPMG echoes employing just the HEMT amplifier, the JPA in non-degenerate mode, the JPA in degenerate mode and a control experiment, see text for details. Solid lines show the data, dashed lines the expected gain in SNR assuming uncorrelated noise. (c) Normalized quadrature noise power spectrum $S_Q(\omega)$ of the resonator at high (red) and low (blue) power corresponding to an average population of 10^6 and 3 photons in the cavity, respectively. Both bright and dark gray traces show the corresponding off-resonant noise traces for comparison.

we attribute the sensitivity saturation in the echo signal to phase noise of our resonator. Figure 4(c) presents the normalized on and off resonance quadrature noise power spectra $S_Q(\omega)$ of the out-of-phase quadrature³⁹ for two different powers. The noise originating from the resonator (blue and red line) shows a $S_Q(\omega) \propto 1/\omega$ dependence dominating the background white noise (gray and black line). For the low power measurement (blue line), corresponding to an average population of 3 photons in the resonator, we obtain a rms frequency noise of 7 kHz, which is 7% of κ_l . This amount of phase noise is commonly observed in superconducting micro-resonators³⁹. Compared to low power, the high power spectrum (red line), corresponding to an average population of 10^6 photons, shows significantly less noise and we find that $S_Q(\omega)$ scales with the square-root of the intra-cavity power^{29,39}. This suggests that origin of the low frequency excess noise lies in the presence of dielectric and/or paramagnetic defects⁴⁰⁻⁴⁸.

In conclusion, we have presented spin-echo measurements with a sensitivity of 65 spins/ $\sqrt{\text{Hz}}$, setting a new state-of-the-art for inductively-detected EPR. This was obtained by employing a low mode volume planar superconducting resonator in conjunction with a quantum limited detection chain. The energy lifetime of the spins

was limited by the Purcell effect to 20 ms, allowing for fast repeating measurements. Due to the long coherence time of the spin system under investigation, Bi donors in ^{28}Si , it was possible to enhance the sensitivity further by a CPMG sequence to $33\text{ spins}/\sqrt{\text{Hz}}$. Achieving the maximum theoretical sensitivity with CPMG of $11\text{ spins}/\sqrt{\text{Hz}}$ was most likely hindered by the phase noise of the resonator. These experiments present a further step towards single-spin sensitivity, and the sub-pico-liter detection volume of our spectrometer makes it an interesting tool for investigating paramagnetic surfaces and, in particular, recently discovered 2D materials^{49,50}.

We acknowledge technical support from P. Sénat and P.-F. Orfila, as well as useful and stimulating discussions within the Quantronics group. We acknowledge support of the European Research Council under the European Community's Seventh Framework Programme (FP7/2007-2013) through grant agreements No. 615767 (CIRQUSS), 279781 (ASCENT), and 630070 (quRAM), and of the ANR project QIPSE as well as the the Villum Foundation.

- ¹A. Schweiger and G. Jeschke, *Principles of pulse electron paramagnetic resonance* (Oxford University Press, 2001).
- ²X-band frequency range: 8 to 12 GHz.
- ³J. Wrachtrup, C. Von Borczyskowski, J. Bernard, M. Orritt, and R. Brown, *Nature* **363**, 244 (1993).
- ⁴A. Gruber, A. Dräbenstedt, C. Tietz, L. Fleury, J. Wrachtrup, and C. v. Borczyskowski, *Science* **276**, 1212 (1997), <http://science.sciencemag.org/content/276/5321/1212.full.pdf>.
- ⁵S. Baumann, W. Paul, T. Choi, C. P. Lutz, A. Ardavan, and A. J. Heinrich, *Science* **350**, 417 (2015).
- ⁶Y. Manassen, R. J. Hamers, J. E. Demuth, and A. J. Castellano Jr., *Phys. Rev. Lett.* **62**, 2531 (1989).
- ⁷D. Rugar, C. Yannoni, and J. Sidles, *Nature* **360**, 563 (1992).
- ⁸D. Rugar, R. Budakian, H. Mamin, and B. Chui, *Nature* **430**, 329 (2004).
- ⁹M. Grinolds, M. Warner, K. De Greve, Y. Dovzhenko, L. Thiel, R. Walsworth, S. Hong, P. Maletinsky, and A. Yacoby, *Nature nanotechnology* **9**, 279 (2014).
- ¹⁰R. V. Chamberlin, L. A. Moberly, and O. G. Symko, *Journal of Low Temperature Physics* **35**, 337 (1979).
- ¹¹F. Hoehne, L. Dreher, J. Behrends, M. Fehr, H. Huebl, K. Lips, A. Schnegg, M. Suckert, M. Stutzmann, and M. S. Brandt, *Review of Scientific Instruments* **83**, 043907 (2012).
- ¹²A. Morello, J. J. Pla, F. A. Zwanenburg, K. W. Chan, K. Y. Tan, H. Huebl, M. Möttönen, C. D. Nugroho, C. Yang, J. A. van Donkelaar, *et al.*, *Nature* **467**, 687 (2010).
- ¹³R. Narkowicz, D. Suter, and I. Niemeyer, *Review of Scientific Instruments* **79**, 084702 (2008), <http://dx.doi.org/10.1063/1.2964926>.
- ¹⁴L. Shtirberg, Y. Twig, E. Dikarov, R. Halevy, M. Levit, and A. Blank, *Review of Scientific Instruments* **82**, 043708 (2011), <http://dx.doi.org/10.1063/1.3581226>.
- ¹⁵Y. Kubo, I. Diniz, C. Grezes, T. Umeda, J. Isoya, H. Sumiya, T. Yamamoto, H. Abe, S. Onoda, T. Ohshima, V. Jacques, A. Dréau, J.-F. Roch, A. Auffeves, D. Vion, D. Esteve, and P. Bertet, *Phys. Rev. B* **86**, 064514 (2012).
- ¹⁶H. Malissa, D. I. Schuster, A. M. Tyryshkin, A. A. Houck, and S. A. Lyon, *Review of Scientific Instruments* **84**, 025116 (2013), <http://dx.doi.org/10.1063/1.4792205>.
- ¹⁷A. J. Sigillito, H. Malissa, A. M. Tyryshkin, H. Riemann, N. V. Abrosimov, P. Becker, H.-J. Pohl, M. L. W. Thewalt, K. M. Itoh, J. J. L. Morton, A. A. Houck, D. I. Schuster, and S. A. Lyon, *Applied Physics Letters* **104**, 222407 (2014).
- ¹⁸A. Bienfait, J. Pla, Y. Kubo, M. Stern, X. Zhou, C.-C. Lo, C. Weis, T. Schenkel, M. Thewalt, D. Vion, D. Esteve, B. Julsgaard, K. Moelmer, J. Morton, and P. Bertet, *Nature Nanotechnology* **11**, 253 (2015).
- ¹⁹A. Bienfait, P. Campagne-Ibarcq, A. Holm-Kiüllerich, X. Zhou, S. Probst, J. J. Pla, T. Schenkel, D. Vion, D. Esteve, J. J. L. Morton, K. Moelmer, and P. Bertet, “Magnetic resonance with squeezed microwaves,” (2016), [arXiv:1610.03329](https://arxiv.org/abs/1610.03329).
- ²⁰C. Eichler, A. J. Sigillito, S. A. Lyon, and J. R. Petta, *Phys. Rev. Lett.* **118**, 037701 (2017).
- ²¹M. H. Devoret and R. J. Schoelkopf, *Science* **339**, 1169 (2013), <http://science.sciencemag.org/content/339/6124/1169.full.pdf>.
- ²²P. Haikka, Y. Kubo, A. Bienfait, P. Bertet, and K. Mølmer, *Phys. Rev. A* **95**, 022306 (2017).
- ²³X. Zhou, V. Schmitt, P. Bertet, D. Vion, W. Wustmann, V. Shumeiko, and D. Esteve, *Phys. Rev. B* **89**, 214517 (2014).
- ²⁴C. M. Caves, *Phys. Rev. D* **26**, 1817 (1982).
- ²⁵T. Yamamoto, K. Inomata, M. Watanabe, K. Matusuba, T. Miyazaki, W. D. Oliver, Y. Nakamura, and J. S. Tsai, *Applied Physics Letters* **93**, 042510 (2008), <http://dx.doi.org/10.1063/1.2964182>.
- ²⁶S. Haroche and J.-M. Raimond, *Exploring the Quantum* (Oxford University Press, 2006).
- ²⁷D. M. Pozar, *Microwave Engineering* (Wiley, 4 edition, 2011).
- ²⁸S. Probst, F. B. Song, P. A. Bushev, A. V. Ustinov, and M. Weides, *Review of Scientific Instruments* **86**, 024706 (2015), <http://dx.doi.org/10.1063/1.4907935>.
- ²⁹A. D. O’Connell, M. Ansmann, R. C. Bialczak, M. Hofheinz, N. Katz, E. Lucero, C. McKenney, M. Neeley, H. Wang, E. M. Weig, A. N. Cleland, and J. M. Martinis, *Applied Physics Letters* **92**, 112903 (2008), <http://dx.doi.org/10.1063/1.2898887>.
- ³⁰G. Feher, *Phys. Rev.* **114**, 1219 (1959).
- ³¹G. W. Morley, M. Warner, A. M. Stoneham, P. T. Greenland, J. van Tol, C. W. Kay, and G. Aeppli, *Nature materials* **9**, 725 (2010).
- ³²G. Wolfowicz, A. M. Tyryshkin, R. E. George, H. Riemann, N. V. Abrosimov, P. Becker, H.-J. Pohl, M. L. W. Thewalt, S. a. Lyon, and J. J. L. Morton, *Nature Nanotechnology* **8**, 561 (2013).
- ³³A. Bienfait, P. Campagne-Ibarcq, A. Holm-Kiüllerich, X. Zhou, S. Probst, J. J. Pla, T. Schenkel, D. Vion, D. Esteve, J. J. L. Morton, K. Moelmer, and P. Bertet, “Magnetic resonance with squeezed microwaves,” (2016), [arXiv:1610.03329](https://arxiv.org/abs/1610.03329).
- ³⁴A. Bienfait, J. Pla, Y. Kubo, X. Zhou, M. Stern, C.-C. Lo, C. Weis, T. Schenkel, D. Vion, D. Esteve, J. Morton, and P. Bertet, *Nature* **531**, 74 (2016).
- ³⁵J. J. Pla, A. Bienfait, G. Pica, J. Mansir, F. A. Mohiyaddin, A. Morello, T. Schenkel, B. W. Lovett, J. J. L. Morton, and P. Bertet, “Strain-induced nuclear quadrupole splittings in silicon devices,” (2016), [arXiv:1608.07346](https://arxiv.org/abs/1608.07346).
- ³⁶T. Thorbeck and N. M. Zimmerman, *AIP Advances* **5**, 087107 (2015).
- ³⁷J. Mansir *et al.*, in preparation (2017).
- ³⁸F. Mentink-Vigier, A. Collauto, A. Feintuch, I. Kaminker, V. Tarle, and D. Goldfarb, *Journal of Magnetic Resonance* **236**, 117 (2013).
- ³⁹J. Gao, J. Zmuidzinas, B. A. Mazin, H. G. LeDuc, and P. K. Day, *Applied Physics Letters* **90**, 102507 (2007).
- ⁴⁰S. E. de Graaf, A. A. Adamyan, T. Lindström, D. Erts, S. E. Kubatkin, A. Y. Tzalenchuk, and A. V. Danilov, *Phys. Rev. Lett.* **118**, 057703 (2017).
- ⁴¹S. E. de Graaf, L. Faoro, J. Burnett, A. A. Adamyan, A. Y. Tzalenchuk, S. E. Kubatkin, T. Lindström, and A. V. Danilov, “Suppression of 1/f noise in solid state quantum devices by surface spin desorption,” (2017), [arXiv:1705.09158](https://arxiv.org/abs/1705.09158).
- ⁴²E. Paladino, Y. M. Galperin, G. Falci, and B. L. Altshuler, *Rev. Mod. Phys.* **86**, 361 (2014).
- ⁴³C. Wang, C. Axline, Y. Y. Gao, T. Brecht, Y. Chu, L. Frunzio, M. H. Devoret, and R. J. Schoelkopf, *Applied Physics Letters*

- 107**, 162601 (2015), <http://dx.doi.org/10.1063/1.4934486>.
- ⁴⁴J. Gao, M. Daal, A. Vayonakis, S. Kumar, J. Zmuidzinas, B. Sadoulet, B. A. Mazin, P. K. Day, and H. G. Leduc, *Applied Physics Letters* **92**, 152505 (2008), <http://dx.doi.org/10.1063/1.2906373>.
- ⁴⁵P. Macha, S. H. W. van der Ploeg, G. Oelsner, E. Ilichev, H.-G. Meyer, S. Wnsch, and M. Siegel, *Applied Physics Letters* **96**, 062503 (2010), <http://dx.doi.org/10.1063/1.3309754>.
- ⁴⁶S. Sendelbach, D. Hover, A. Kittel, M. Mück, J. M. Martinis, and R. McDermott, *Phys. Rev. Lett.* **100**, 227006 (2008).
- ⁴⁷J. Burnett, L. Faoro, I. Wisby, V. L. Gurtovoi, A. V. Chernykh, G. M. Mikhailov, V. A. Tulin, R. Shaikhaidarov, V. Antonov, P. J. Meeson, A. Y. Tzalenchuk, and T. Lindström, **5**, 4119 (2014).
- ⁴⁸S. M. Anton, J. S. Birenbaum, S. R. O'Kelley, V. Bolkhovsky, D. A. Braje, G. Fitch, M. Neeley, G. C. Hilton, H.-M. Cho, K. D. Irwin, F. C. Wellstood, W. D. Oliver, A. Shnirman, and J. Clarke, *Phys. Rev. Lett.* **110**, 147002 (2013).
- ⁴⁹A. K. Geim and I. V. Grigorieva, *Nature* **499**, 419 (2013).
- ⁵⁰K. S. Novoselov, A. Mishchenko, A. Carvalho, and A. H. Castro Neto, *Science* **353** (2016), [10.1126/science.aac9439](https://doi.org/10.1126/science.aac9439).